Molecular Cell

Article

A recurrent chromosomal inversion suffices for driving escape from oncogene-induced senescence via subTAD reorganization

Graphical abstract

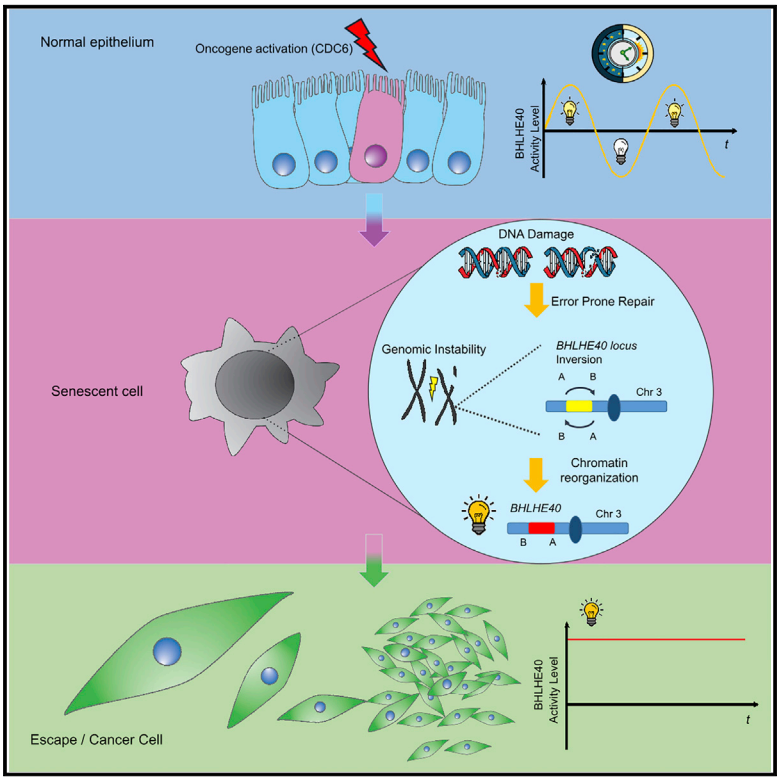

Highlights

- Oncogene-driven repair produces early genetic lesions, allowing escape from senescence
- Cells escaping senescence display mutational signatures observed in individuals with cancer
- A recurrent inversion harboring a circadian gene suffices for bypassing senescence
- Chromatin loop and compartment remodeling support the "escape" transcriptional program

Authors

Christos P. Zampetidis, Panagiotis Galanos, Andriani Angelopoulou, ..., Jiri Bartek, Argyris Papantonis, Vassilis G. Gorgoulis

Correspondence

panos@cancer.dk (P.G.), jb@cancer.dk (J.B.), argyris.papantonis@med.uni-goettingen.de (A.P.), vgorg@med.uoa.gr (V.G.G.)

In brief

Zampetidis et al. demonstrate that a recurrent chromosomal inversion harboring the circadian gene *BHLHE40* is sufficient to drive escape from oncogene-induced senescence. The inversion is the outcome of oncogene-mediated genomic instability followed by chromatin refolding changes that activate the gene, leading to cell cycle re-entry and aggressive behavior.

Zampetidis et al., 2021, Molecular Cell *81*, 4907–4923
December 2, 2021
https://doi.org/10.1016/j.molcel.2021.10.017

CellPress

Molecular Cell

CellPress

Article

A recurrent chromosomal inversion suffices for driving escape from oncogene-induced senescence via subTAD reorganization

Christos P. Zampetidis,[1,17] Panagiotis Galanos,[2,17,*] Andriani Angelopoulou,[1,17] Yajie Zhu,[3] Aikaterini Polyzou,[1] Timokratis Karamitros,[4] Athanassios Kotsinas,[1] Nefeli Lagopati,[1] Ioanna Mourkioti,[1] Reza Mirzazadeh,[5] Alexandros Polyzos,[6] Silvano Garnerone,[5] Athanasia Mizi,[3] Eduardo G. Gusmao,[3] Konstantinos Sofiadis,[3] Zita Gál,[7] Dorthe H. Larsen,[7] Dafni-Eleftheria Pefani,[8] Marco Demaria,[9] Aristotelis Tsirigos,[10] Nicola Crosetto,[5] Apolinar Maya-Mendoza,[11] Angelos Papaspyropoulos,[1] Konstantinos Evangelou,[1] Jiri Bartek,[2,5,*] Argyris Papantonis,[3,12,*] and Vassilis G. Gorgoulis[1,13,14,15,16,18,*]

[1]Molecular Carcinogenesis Group, Department of Histology and Embryology, Faculty of Medicine, National Kapodistrian University of Athens, 11527 Athens, Greece

[2]Genome Integrity Group, Danish Cancer Society Research Center, 2100 Copenhagen, Denmark

[3]Translational Epigenetics Group, Institute of Pathology, University Medical Center Göttingen, 37075 Göttingen, Germany

[4]Unit of Bioinformatics and Applied Genomics, Department of Microbiology, Hellenic Pasteur Institute, 11521 Athens, Greece

[5]Science for Life Laboratory, Division of Genome Biology, Department of Medical Biochemistry and Biophysics, Karolinska Institute, 171 77 Solna, Stockholm, Sweden

[6]Sanford I. Weill Department of Medicine, Sandra and Edward Meyer Cancer Center, Weill Cornell Medicine, New York, NY 10065, USA

[7]Nucleolar Stress and Disease Group, Danish Cancer Society Research Center, 2100 Copenhagen, Denmark

[8]Laboratories of Biology, Medical School, University of Patras, 26504 Rio, Greece

[9]University of Groningen (RUG), European Research Institute for the Biology of Aging (ERIBA), University Medical Center Groningen (UMCG), 9713 AV Groningen, the Netherlands

[10]Department of Pathology, NYU School of Medicine, New York, NY 10016, USA

[11]DNA Replication and Cancer Group, Danish Cancer Society Research Center, 2100 Copenhagen, Denmark

[12]Center for Molecular Medicine Cologne (CMMC), University of Cologne, 50931 Cologne, Germany

[13]Biomedical Research Foundation, Academy of Athens, 11527 Athens, Greece

[14]Division of Cancer Sciences, School of Medical Sciences, Faculty of Biology, Medicine & Health, University of Manchester, M20 4GJ Manchester, UK

[15]Center for New Biotechnologies and Precision Medicine, Medical School, National and Kapodistrian University of Athens, 11527 Athens, Greece

[16]Faculty of Health and Medical Sciences, University of Surrey, Surrey GU2 7YH, UK

[17]These authors contributed equally

[18]Lead contact

*Correspondence: panos@cancer.dk (P.G.), jb@cancer.dk (J.B.), argyris.papantonis@med.uni-goettingen.de (A.P.), vgorg@med.uoa.gr (V.G.G.)

https://doi.org/10.1016/j.molcel.2021.10.017

SUMMARY

Oncogene-induced senescence (OIS) is an inherent and important tumor suppressor mechanism. However, if not removed timely via immune surveillance, senescent cells also have detrimental effects. Although this has mostly been attributed to the senescence-associated secretory phenotype (SASP) of these cells, we recently proposed that "escape" from the senescent state is another unfavorable outcome. The mechanism underlying this phenomenon remains elusive. Here, we exploit genomic and functional data from a prototypical human epithelial cell model carrying an inducible *CDC6* oncogene to identify an early-acquired recurrent chromosomal inversion that harbors a locus encoding the circadian transcription factor BHLHE40. This inversion alone suffices for *BHLHE40* activation upon *CDC6* induction and driving cell cycle re-entry of senescent cells, and malignant transformation. Ectopic overexpression of BHLHE40 prevented induction of CDC6-triggered senescence. We provide strong evidence in support of replication stress-induced genomic instability being a causative factor underlying "escape" from oncogene-induced senescence.

INTRODUCTION

According to the DNA damage model for cancer development, activated oncogenes trigger genomic instability that, at some point, breaches the tumor-suppressing barriers of apoptosis and senescence to promote cancer development (Halazonetis et al., 2008). This model readily explains how emerging genomic instability in cancer leads to evasion of apoptosis via

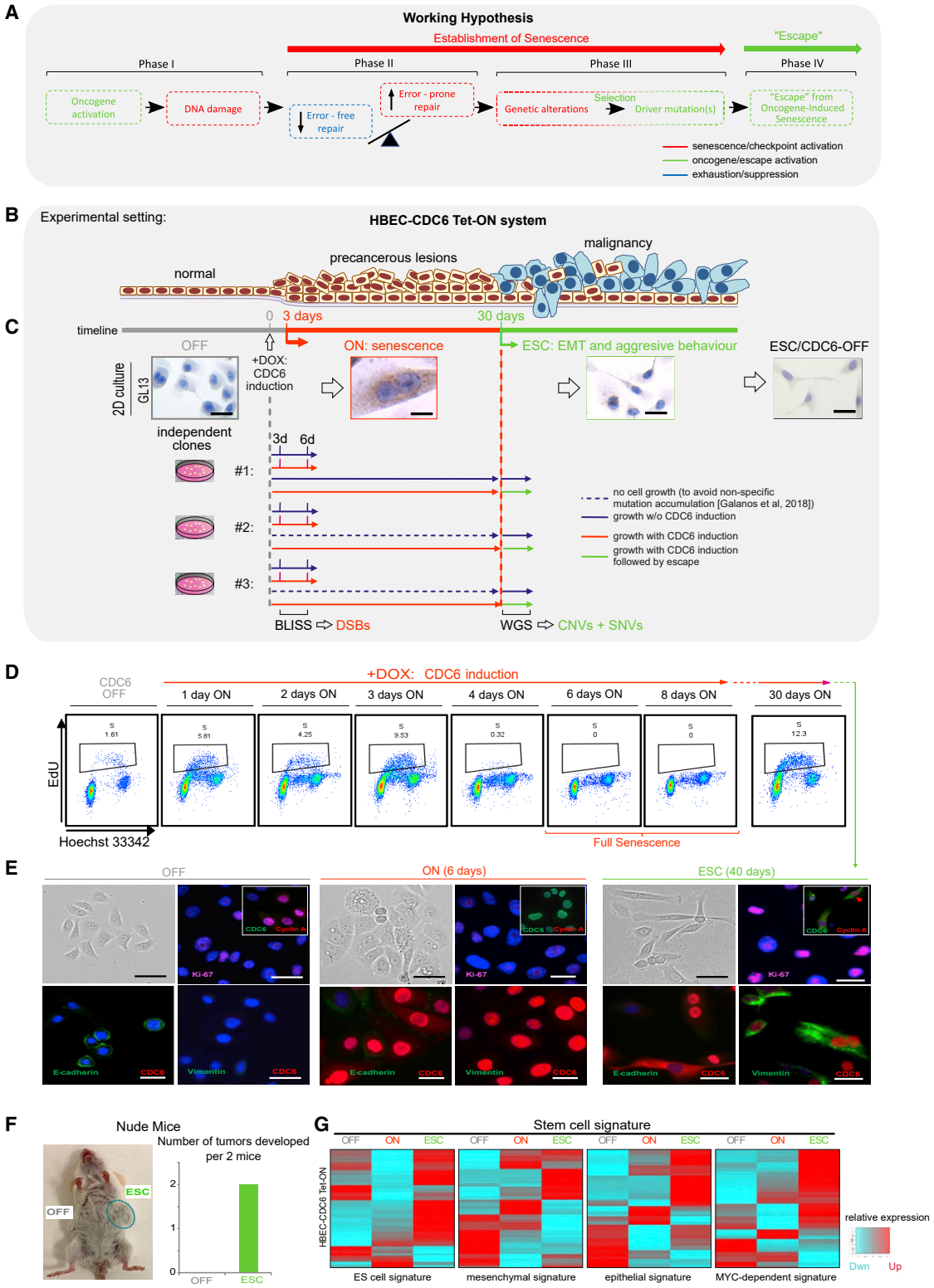

Figure 1. ESC from OIS

(A) Working hypothesis, based on our cancer development model (Halazonetis et al., 2008), to address the aim of this study: showing that accumulating DNA damage traits during oncogene-induced senescence (OIS) will be selected and should appear in ESC cells as functionally meaningful genetic defects.

(B) A human bronchial epithelial cell (HBEC) *CDC6*-TetON cellular system recapitulating successive stages of cancer evolution (Komseli et al., 2018).

(legend continued on next page)

accumulation of inactivating mutations at key signaling hubs and regulatory factors (Halazonetis et al., 2008; Negrini et al., 2010; Gorgoulis et al., 2018). It also provides the basis for considering senescence as an inherent barrier to tumor development in precancerous stages (Bartkova et al., 2006; Di Micco et al., 2006; Collado et al., 2005; Braig et al., 2005; Michaloglou et al., 2005; Chen et al., 2005). However, this model does not explain how cells "escape" from senescence and particularly how cells that have entered such a state of irreversible cell cycle arrest become able to breach this barrier and re-initiate proliferation.

Recently, we and others demonstrated that a subset of cells in a senescent population do re-enter the cell cycle, "escaping" senescence (Galanos et al., 2016, 2018; Yu et al., 2018; Milanovic et al., 2018; Patel et al., 2016). Such "escapee" cells adopt a more aggressive phenotype that closely mimics cancer development (Gorgoulis et al., 2019). The molecular mechanism underlying this "escape" phenomenon has not yet been deciphered.

Here we hypothesize that, if our cancer development model (Halazonetis et al., 2008) also applies to the "escape" phenomenon, then accumulating DNA damage traits during oncogene-induced senescence (OIS) would be selected and should appear in "escape" cells as functionally meaningful genetic aberrations (Figure 1A). To address this, we combine a prototypical human epithelial OIS cellular system with genomics and functional assays to present the first evidence in support of this hypothesis and discuss its clinical significance.

RESULTS

An OIS model recapitulating cancer evolution

We recently described a cellular system based on normal human bronchial epithelial cells (HBECs) carrying a *CDC6*-TetON overexpression cassette (Figure 1B; Moreno et al., 2016; Komseli et al., 2018). HBECs are of epithelial origin, like most common cancer types, and in their uninduced state ("OFF" in Figure 1B), they are free from the mutation burden found in cancer cells (Goodspeed et al., 2016; Stratton et al., 2009). This permits accurate detection of amassing DNA alterations during *CDC6*-induced senescence ("ON" state in Figure 1B).

The replication licensing factor CDC6 was chosen as the inducible oncogenic stimulus because (1) as a key component of the replication licensing machinery integrating most mitogenic and oncogenic stimuli, it is frequently deregulated, also by gene amplification, from the earliest stages of cancer (Karakaidos et al., 2004; Liontos et al., 2007; Sideridou et al., 2011; Petrakis et al., 2016); (2) compared to other tested oncogenes, such as *RAS* or *BRAF*, it is a more powerful inducer of senescence (Patel et al., 2016); and (3) its overexpression is linked to poor survival across common cancer types (Figure S1A).

Importantly, this system offers the advantage of prompt and quantitative senescence entry (< 6 days), followed by escape from senescence in a reasonably short time period (within ~30 days; escape [ESC]; Figures 1B and S1B; Moreno et al., 2016; Komseli et al., 2018). These transitions recapitulate the whole evolution course of malignant transformation and can be observed equally under 2D and 3D organotypic cell culture conditions (Figures 1B, 1C, and S1C). Thus, for our working hypothesis (Introduction) to be validated, the following sequence of steps (phases) initiated by an oncogenic insult are predicted to occur (Figure 1A).

First, shutting off *CDC6* overexpression in cells that have "escaped" senescence should not result in phenotype reversal, suggesting acquisition of permanent molecular alterations. Second, following *CDC6* induction, DNA double-strand breaks (DSBs) should form (phase I; Figure 1A), and at least a fraction of them should be repaired in an error-prone manner (phase II; Figure 1A). Third, some genomic alterations produced in the senescent state (phase III; Figure 1A) should be selected for to functionally facilitate ESC (phase IV; Figure 1A).

CDC6 expression is dispensable after EMT-like ESC from senescence

To exclude mapping of stochastic alterations, we conducted three independent evolution experiments (Figure 1C). In all three experiments, a fraction of cells (~50 colonies from 5×10^5 cells) re-entered the cell cycle after the protracted CDC6-induced senescent phase (Figure 1D; Videos S1 and S2). These ESC cells grew faster, were invasive, and adopted epithelial-to-mesenchymal transition (EMT) features (Figures 1C–1E and S1D–S1F; Videos S1 and S2) known to facilitate cancer progression (Nieto et al., 2016; Thiery et al., 2009). They also produced tumors upon injection into nude mice (Figure 1F). Moreover, bioinformatics analysis revealed that the ESC cells exhibited a mixed stem cell-like gene expression signature encompassing embryonic, epithelial, mesenchymal-like, and MYC-dependent markers (Ritschka et al., 2017; Wong et al., 2008; Kim et al., 2010; Ivanova et al., 2002; Chambers et al., 2007; Milanovic et al., 2018;

(C) Representative images of HBECs grown in 2D culture and stained for GL13 (SenTraGor). *CDC6* induction forces cells into senescence (ON). After ~30 days, a subset of cells "escape" senescence (ESC) to re-enter the cell cycle and adopt an EMT phenotype. Shutting off *CDC6* in ESC cells (ESC/*CDC6*-OFF) does not reverse this phenotype. Shown is an overview of three independent ESC experiments. BLISS was applied to identify DSBs occurring after 3 or 6 days of CDC6 induction. Then, whole-genome sequencing (WGS) was performed on ESC cells to map genetic alterations with respect to damage that occurred at early time points. OFF cells that served as controls for WGS analysis were only initiated for culture when ESC cells emerged to avoid non-specific accumulation of genetic alterations in the prolonged stationary period of senescent ON cells. Scale bars: 20 μm (OFF), 10 μm (ON), and 20 μm (ESC and ESC/*CDC6*-OFF).
(D) FACS-based cell cycle analysis of HBECs at different time points, following 5-ethynyl-2′-deoxyuridine (EdU) incorporation and *CDC6* induction, demonstrating progressive S-phase reduction, acquisition of senescence, and ESC.
(E) Representative phase contrast views and immunodetection of epithelial (E-cadherin) and mesenchymal markers (vimentin) in HBECs, showing that senescence "escape" (ESC) coincides with EMT. Scale bars: 20 μm (OFF) and 15 μm (ON and ESC).
(F) Tumorigenicity assay of ESC and OFF cells in severe combined immunodeficiency (SCID) mice and histological analysis of the tumors that developed (right).
(G) Heatmaps showing that ESC cells display a mixed stem cell-like gene expression signature consisting of embryonic, mesenchymal, epithelial, and Myc-dependent markers (for references, see text).

Figure 1G). Notably, switching off *CDC6* overexpression does not result in ESC phenotype reversal, preserving the growth and invasion capacity of the "escapee" cells, in line with our hypothesis (Figures 1B, 1C, and S1D–S1F).

DSBs occur early upon senescence entry and are repaired in an error-prone manner

We suspected that, as a licensing factor, deregulated CDC6 would alter replication dynamics and induce replication stress. In turn, replication stress could lead to accumulation of breaks on the DNA (Halazonetis et al., 2008). To determine whether and to what extent DNA DSBs occur, we performed BLISS (breaks labeling *in situ* and sequencing) analysis (Yan et al., 2017) at different time points after *CDC6* overexpression (Figure 1C). BLISS data analysis verified DSBs emergence, with a dramatic increase 3 days after *CDC6* -induced senescence entry and an almost 50% reduction at the peak of senescence (day 6), suggesting that a repair process took place (Figure 2A).

To mechanistically explain DSB formation, we analyzed the classic markers of replication stress. We found strong aberrations in the form of reduced fork speed and asymmetry following *CDC6* induction (Figure 2B). In addition, the fraction of cells with increased DNA content (>4N) and DNA damage marker expression, indicative of re-replication (Galanos et al., 2018; Petrakis et al., 2016), increased progressively (Figures 1D, 2C, and S2). Given that DSBs detected by BLISS were particularly enriched at transcription start sites (TSSs) (Figures 2D and 2E; in agreement with previous observations by Gothe et al., 2019), we postulated that replication-transcription collisions could occur at these positions. In line with this, global inhibition of transcriptional elongation by RNA polymerase II (RNAPII) using 5,6-dichloro-1-β-D-ribofuranosylbenzimidazole (DRB) significantly reduced the levels of DNA damage response (DDR) (Figure 2F). Our results showed that overexpression of CDC6 induced replication stress, accumulation of DSBs, and DNA damage response, validating phase I of our hypothesis (Figure 1A).

Next, we investigated the choice of repair pathway for the CDC6-induced DNA breaks. Concurrent with DSB emergence, we recorded a prompt (within ~24 h) and robust increase in RPA foci (Figures 3Ai, 3Aii, and S2), a single-strand DNA binding factor and surrogate marker for replication stress (Gorgoulis et al., 2018). This finding, in combination with our BLISS results, suggested that repair may take place predominantly via homologous recombination (HR) during S phase and before the peak of senescence establishment. However, the levels of key components of the main error-free HR pathway, synthesis-dependent strand annealing (SDSA), like RAD51, BRCA1, and BRCA2, are reduced after the third day of CDC6 induction (Figures 3Bi and 3Bii). In contrast, RAD52 levels and foci increased upon *CDC6* overexpression between days 3 and 6 (Figures 3Bii and 3Ci–3Ciii). Thus, in this conditional "BRCAness" environment with low RAD51 levels (Wu et al., 2008; Ochs et al., 2016; Galanos et al., 2016, 2018; Gorgoulis et al., 2018;), DNA repair will predominantly rely on RAD52 activity, which is central to break-induced-replication (BIR) and single-strand-annealing (SSA) repair pathways. BIR and SSA are highly error-prone mechanisms contributing to genomic instability and oncogenic transformation (Galanos et al., 2016, 2018; Sotiriou et al., 2016), and we found them to be activated significantly in ON cells in a RAD52-dependent manner (Figure 3D). At the same time, SDSA processivity was reduced strongly, satisfying the requirement for phase II of our working hypothesis (Figure 1A), as we saw a shift from high- to low-fidelity DSB repair.

ESC cells harbor genomic alterations selected early upon senescence entry

Following a senescent period of ~4 weeks, ESC clones emerged in all three replicates (Figures 1B–1E, S1B, and S1C). To examine whether traits of DNA damage produced early in senescence are selected and maintained in ESC populations, we employed whole-genome sequencing (WGS). Compared with the non-induced cells, WGS uncovered a broad spectrum of single-nucleotide variants (SNVs) and copy number variants (CNVs) (Figures 4A and S3A; Table S1).

Chromosomal distribution of SNVs took a "kataegis" form, and we could deduce a mutation signature (Figures S3B and S3C) resembling the previously reported "signature 15" associated with mismatch defects seen in stomach and lung cancer (Alexandrov et al., 2013). Moreover, SNV analysis revealed that our "cancer evolution" model recapitulated two of the most frequently occurring cancer mutations, in *MUC16* and in *NEB* (Figures S3D–S3F), validating its relevance. Both mutations are associated with poor outcomes in individuals with cancer (Chugh et al., 2015; Kufe, 2009; Mazzoccoli et al., 2017), with *MUC16* (also known as *CA125*) being an established marker for various cancer types, including lung cancer, that is most relevant to our cellular model. Although no mutations were found in the *TP53* gene, the most altered gene in cancer (Figure S3D; Zhu et al., 2020), its negative regulator, MDM2, increases in ESC cells, leading to its downregulation (Figure S4A), providing an alternative mode of p53 attenuation.

Finally, by interrogating the spectrum of recorded CNVs, we made two observations. First, as predicted by our model (Halazonetis et al., 2008; Tsantoulis et al., 2008), genetic alterations were located within common fragile sites (CFSs; Table S1). Second, 58 of ~344 CNVs per clone were shared by all three replicates (Figures 4A–4C; Table S1). Aligning the breakpoints flanking these CNVs, also confirmed by Sanger sequencing (Figure S5), with DSB coordinates obtained by BLISS resulted in a striking overlap for 51 of 58 of them (Figure 4D; Table S1). The cancer-specific mutational signature (Figure S3C), recapitulation of the *MUC16* and *NEB* mutations seen in affected individuals (Figures S3D–S3F), and the 58 shared CNVs identified in ESC cells (Figures 4B and 4C; Table S1) all point to genomic instability as a decisive determinant for "escaping" OIS. These observations are in agreement with phase III of our hypothesis (Figure 1A).

A large chromosomal inversion uncovers a circadian transcription factor as regulator of ESC

A fundamental question of our working hypothesis is whether genetic alterations obtained early in senescence are functionally relevant for ESC from the OIS state (Introduction). We noticed a more than 3.7-Mbp-long heterozygous balanced inversion in the short arm of chromosome 3 (chr3) in our list of 58 recurring CNVs (Figures 4B–4D and 5A; Table S2). Notably, the breaks flanking this inversion were not more prominent compared with

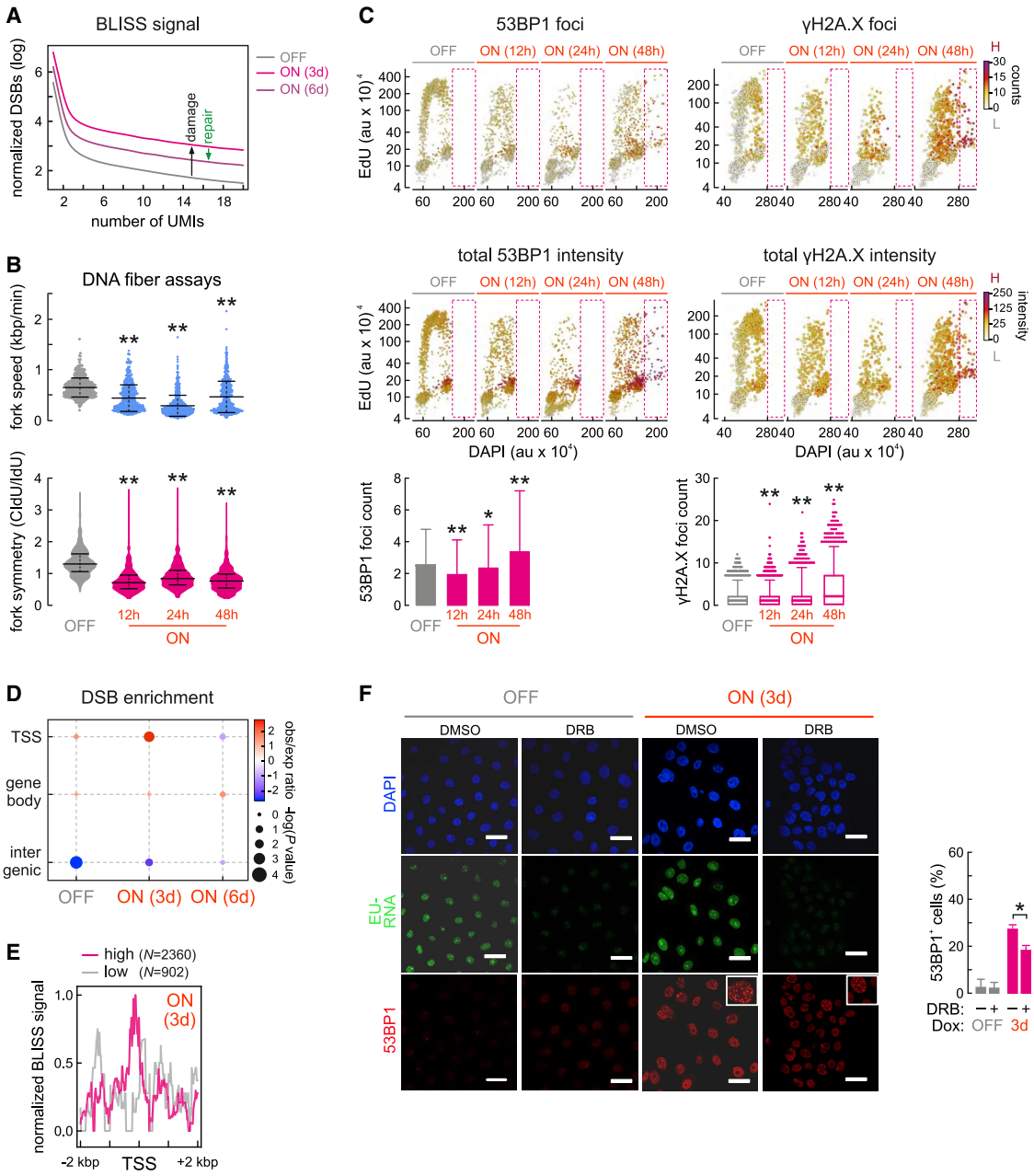

Figure 2. CDC6 induces DNA double-strand breaks (DSBs) and alters replication dynamics

(A) BLISS data generated at the indicated time points after *CDC6* activation show strongest DSBs accumulation at 3 days, followed by 50% reduction at day 6, indicative of DNA repair (UMI, unique molecular identifier).

(B) Violin plots of DNA fiber fluorography results show decreased fork progression rate and asymmetry at the indicated time points. Significantly different from OFF, **p < 0.01; Student's t test (±SD, n = 3).

(C) Quantitative image-based cytometry of HBECs at the indicated time points, showing cell cycle distribution of single cells based on EdU and DAPI levels (a.u., arbitrary unit). Focus counts (top) and 53BP1 and γH2AX levels (center) are indicated by color coding. Bar graphs (bottom) show population means (±SD). Dashed rectangles indicate accumulation of cells with DNA content of more than 4N. Significantly different from OFF, **p < 0.01; Student's t test (±SD, n = 3). H, high level; L, low level.

(D) Dot plot showing increased frequency of DSBs at gene TSSs based on BLISS data.

(E) Histogram showing BLISS-defined DSB enrichment at gene TSSs upon *CDC6* induction.

(F) Representative immunofluorescence imaging (left) of EU-labeled nascent RNA and 53BP1 foci in control HBECs (DMSO) or DRB-treated HBECs to inhibit transcription (DRB) at the indicated times. Bar graphs (right) show the percentage (±SD, n = 3) of cells with 53BP1 foci. Significantly different from OFF, *p < 0.05; two-tailed unpaired Student's t test. Scale bar, 20 μm.

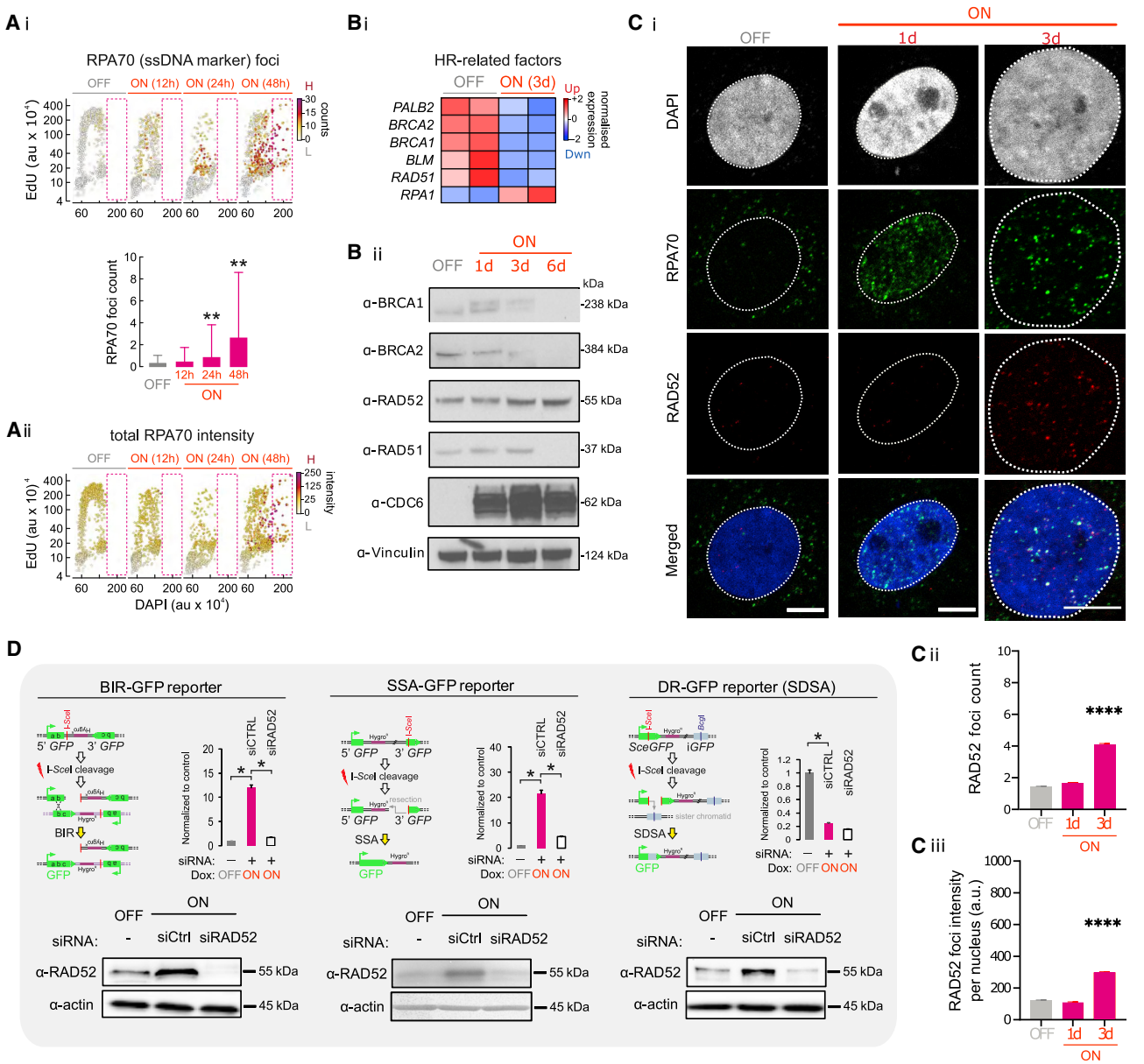

Figure 3. Sustained *CDC6* expression induces replication stress and error-prone DNA repair

(Ai and Aii) Quantitative image-based cytometry of HBECs at the indicated time points shows cell cycle distribution of single cells based on EdU and DAPI levels. Focus counts (top) and RPA70 levels (bottom) are color coded. Bar graphs (center) show population means (±SD, n = 3). Dashed rectangles denote accumulation of cells with DNA content of more than 4N. Significantly different from OFF, **p < 0.01; unpaired two-tailed Student's t test.

(Bi and Bii) Heatmap and western blots showing reduction in the expression levels of the genes involved in error-free homologous recombination (HR) DNA repair upon *CDC6* induction in HBECs (ON). Up, upregulated; Dwn, downregulated.

(C) Immunofluorescence imaging of RAD52 and RPA70 upon CDC6 overexpression in ON cells (i). Bar graphs depict RAD52 mean focus count (ii) and focus intensity (iii) per nucleus, respectively. Significantly different from OFF, ****p < 0.0001, unpaired two-tailed Student's t test. Scale bar, 7 μm.

(D) Reporter assays demonstrating an increase (±SD, n = 3) in RAD52-dependent break-induced replication (BIR; left) and in single-strand annealing (SSA) repair of DSBs (center). Error-free repair monitored by a synthesis-dependent strand annealing (SDSA) reporter (right) is suppressed. Western blots (bottom) depict RAD52 expression levels. *p < 0.05, unpaired two-tailed Student's t test. Repair is monitored 3 days after CDC6 induction.

the breakpoints of the other shared CNVs (Figure 4D) (see Next Generation Sequencing and Bioinformatics analysis for BLISS signal assessment). Naturally occurring inversions are generally less susceptible to further recombination, which suggests that genes within such structural variants are selectively "protected" (Wellenreuther and Bernatchez, 2018). This HBEC-specific inversion encompasses the *BHLHE40* (basic helix-loop-helix family member 40, also known as *DEC1*) locus (Figure 5A), which encodes a transcription factor belonging to the CLOCK (circadian locomotor output cycles kaput) protein family and regulates

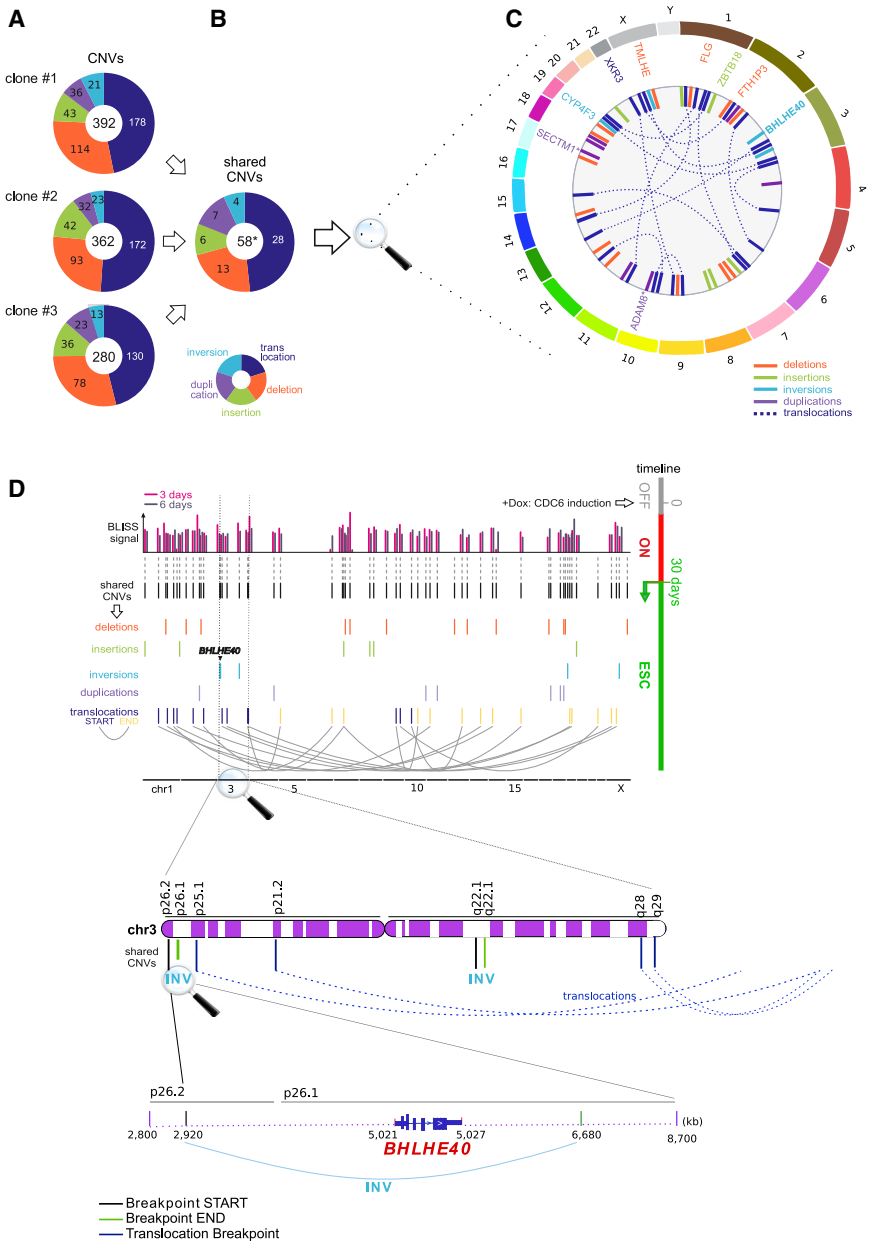

Figure 4. ESC cells harbor recurrent copy number variations (CNVs) aligning with DSBs

(A) Pie charts showing the distribution of CNVs identified in each of three independent replicates in five categories.

(B) Pie charts showing the distribution of the 58 CNVs shared by all the three replicates (Table S1). Significantly more than expected by chance, *p < 0.0001; super exact test.

(C) Circos plot of the type and location of all shared CNVs from (B), alongside any differentially expressed genes they harbor in ESC cells (*, confirmed by qRT-PCR, not in RNA sequencing [RNA-seq] data). Outer circle, human reference karyotype; inner circle, distribution of the 58 CNVs across the genome.

(D) Superimposing DSB coordinates, as defined by BLISS, with the breakpoints of the shared CNVs from (B) shows overlap in 51 of the 58 cases. The inversion in 3p26.1 is magnified.

daily circadian rhythm oscillations (Kato et al., 2014; Sato et al., 2016). Publicly available ENCODE chromatin immunoprecipitation sequencing (ChIP-seq) data reveal that BHLHE40 exhibits strong and ubiquitous binding across the genome and regulates more than 15,500 human genes (Rouillard et al., 2016), including many cell cycle regulators (Figure 5B).

Notably, ~69% of the genes found to be differentially expressed upon ESC from senescence are reported direct BHLHE40 targets, most of them being cell cycle, DNA replication, and repair regulators (Figures 5C and S4B; Tables S4 and S5). Our transcriptome data showed that *BHLHE40* is strongly upregulated in ESC cells (also at the protein level; Figure S4C), whereas *PER1/2*, which encode periodins, the key circadian factors (Yamada and Miyamoto, 2005; Wood et al., 2009; Kato et al., 2014; Sato et al., 2016), and *BHLHE41* are suppressed (Figure 5D). This suggests a direct role of BHLHE40 in promoting ESC. In fact, the circadian circuitry governs, among other processes, cell cycle progression. Therefore, its deregulation affects cell cycle checkpoints and can lead to cancer (Hunt and Sassone-Corsi, 2007; Masri et al., 2013). Looking into genes encoding replication machinery components, we found 38 key ones that are strongly reactivated in ESC cells and bound by BHLHE40 (e.g., *BLM*, *GINS1–GINS4*, *MCM2–MCM10*, *PCNA*, and *POLE*; Figures 5B and 5E). Among these was also MDM2, the main negative regulator of p53 (Figures 5E, S4A, and S4D).

To test the functional significance of BHLHE40 in our working hypothesis, we silenced this gene in ESC cells using small interfering RNAs (siRNAs). This led to a deregulated cell cycle profile and increased cell death, as shown via fluorescence-activated cell sorting (FACS) (from 1.89% ± 0.8% cells to 21.25% ± 0.3%; Figure 5F) and caspase-3 staining (Figure 5G), respectively. Notably, *BHLHE40* silencing also led to upregulation of PER1 (Figure 5H), known to sensitize cells to apoptosis (Gery et al., 2006; Hunt and Sassone-Corsi, 2007). These results show that *BHLHE40* upregulation is necessary for maintenance of the ESC phenotype. BHLHE40 is also relevant for clinical outcomes because its overexpression is associated with adverse effects on survival in various malignancies, including lung cancer (Figure S4E). Notably, the chromosomal region containing *BHLHE40* is prone to genetic aberrations in human malignancies (Figures S3G and S3H; Table S2). Apart from the

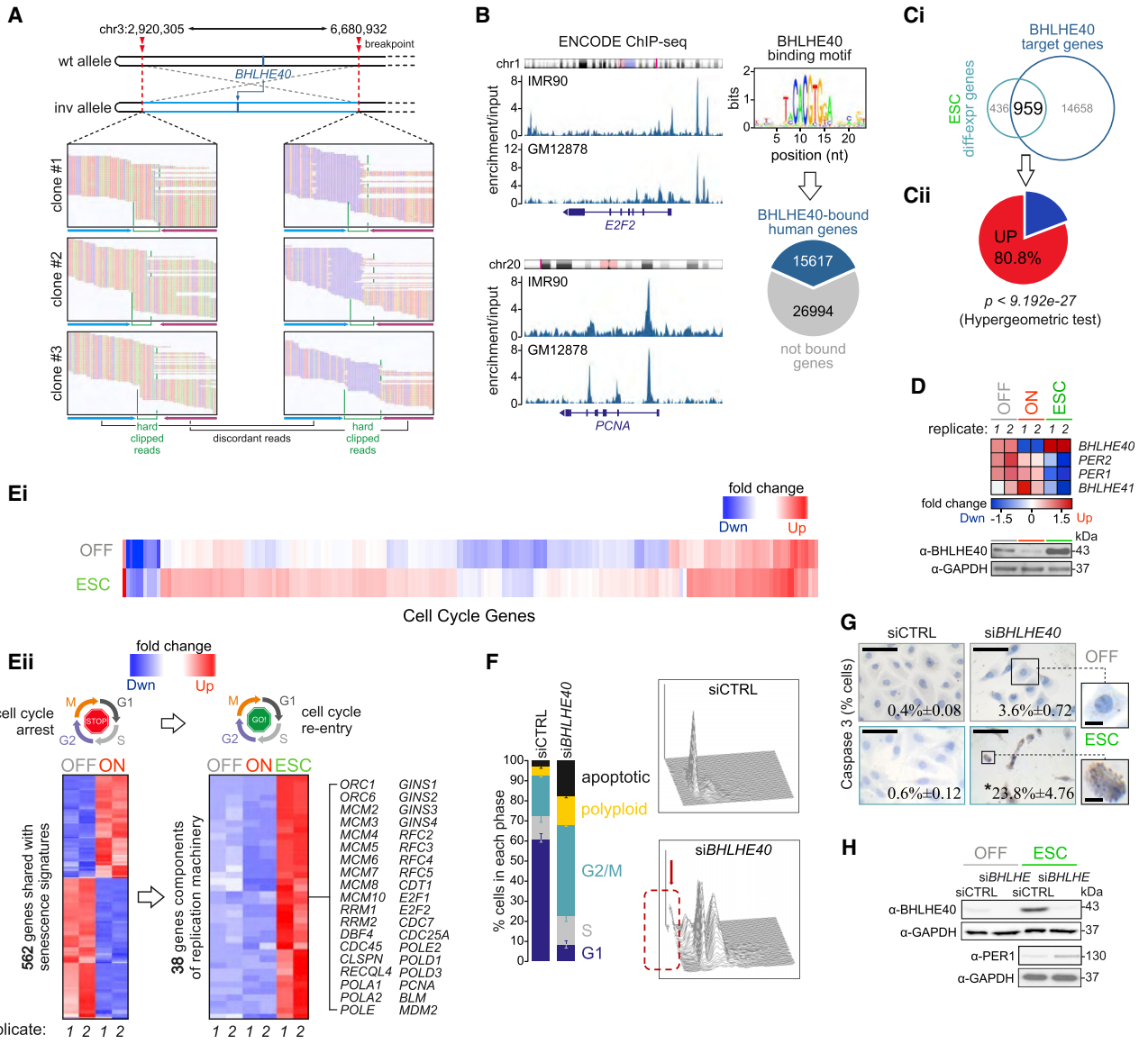

Figure 5. *BHLHE40* harbored in the chr3 inversion is essential for ESC phenotype maintenance

(A) WGS data around the chr3 inversion breakpoints in ESC cells. Hard clipped (green lines) and discordantly mapped reads (blue/purple arrows) are indicated for all three replicates.

(B) Representative genome browser views (left) of BHLHE40 ENCODE ChIP-seq data from IMR90 and GM12878 cells in the *E2F2* and *PCNA* loci. These data were used to infer the BHLHE40 binding motif logo and to assign 36.7% of all human genes as its direct targets (Pertea et al., 2018).

(C) Venn diagram showing that 68.8% of all genes differentially expressed in ESC cells are also BHLHE40 targets according to ChIP-seq data (i). A pie chart shows the significant percentage of the upregulated genes that are identified as BHLHE40 target genes and differentially expressed genes during ESC (ii). $p < 9.192e{-}27$, hypergeometric test.

(D) Heatmap of RNA-seq data shows *BHLHE40*, but not other circadian genes like PER1/2, being selectively upregulated in ESC cells.

(E) Heatmap depicting the fold change expression of cell cycle genes between the ESC and "OFF" conditions (i). Fold change cutoff, 2.0; and p-adjust < 0.05. A heatmap (left) shows that 25.3% of the 2,220 differentially expressed genes in ON cells are shared with reported senescence signatures (Hernandez-Segura et al., 2017) (ii). Of these, 38 encode replication machinery components (right) and are strongly induced in ESC cells.

(F) FACS-based cell cycle profiling of control (siCTRL) and *BHLHE40* knockdown (siBHLHE40) cells showing significantly altered cell cycle progression and increased cell death (red arrow pointing to the dashed line) (±SD, n = 3). Significantly more than in control, *p < 0.001; Fisher's exact test.

(G) Representative images of siCTRL and siBHLHE40 cells immunostained for caspase-3. Inset numbers indicate the percentage of positive cells (from a minimum of 100 cells counted under each condition). *p < 0.01, Fisher's exact test. Scale bars, 25 μm and 5 μm (insets).

(H) Western blots showing reciprocal changes in BHLHE40 and PER1 levels upon *BHLHE40* knockdown in ESC cells, thought to drive apoptosis (Hunt and Sassone-Corsi, 2007).

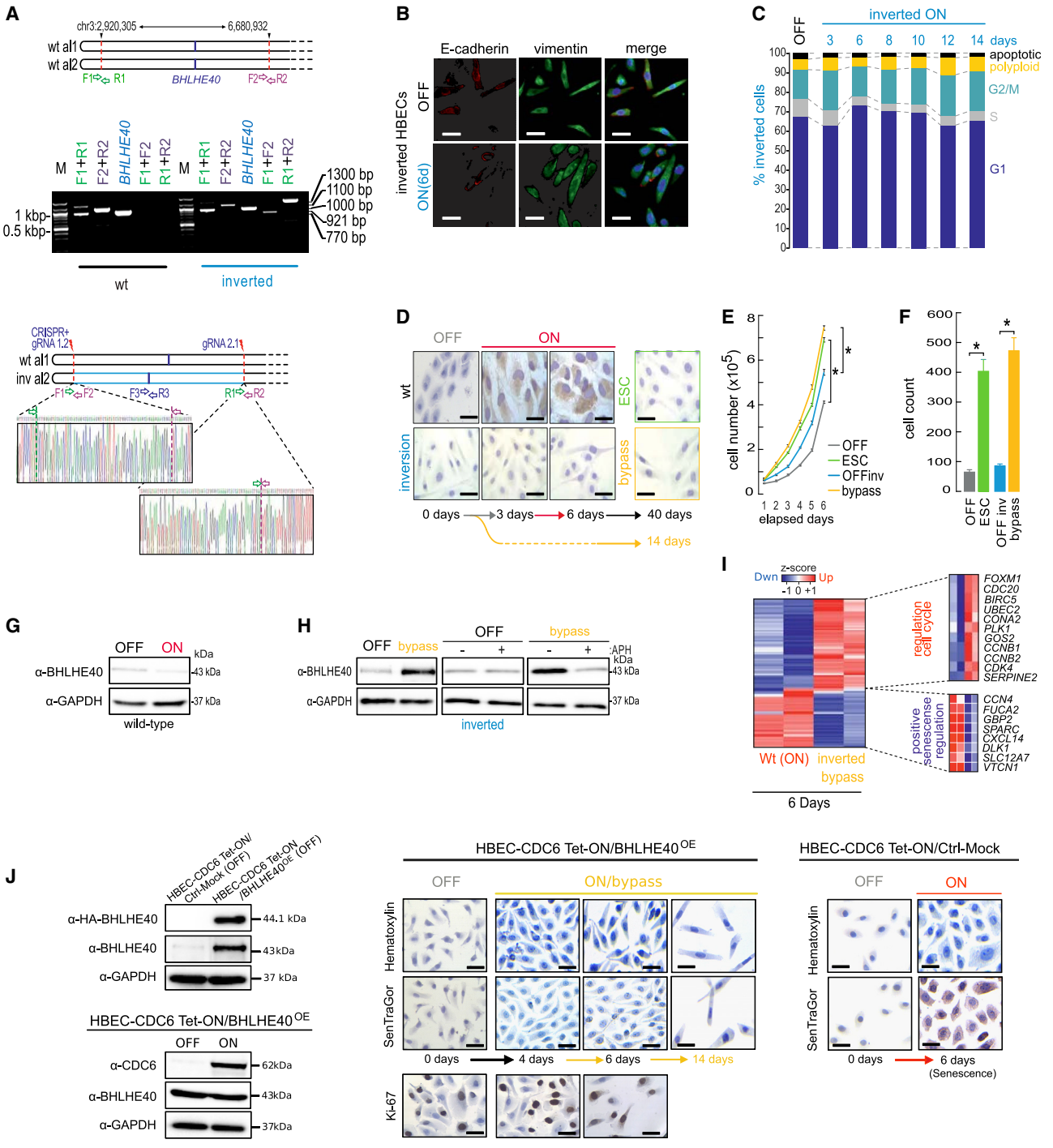

Figure 6. The 3.7-Mbp inversion in chr3 suffices for bypassing CDC6-induced senescence

(A) PCR and Sanger sequencing validation of a CRISPR-generated 3.7-Mbp heterozygous inversion in chr3 that closely mimics that discovered in ESC cells using WGS (WT, wild type). Sanger sequences are available in Table S4D.

(B) Immunodetection of epithelial (E-cadherin) and mesenchymal markers (vimentin) in "inverted" OFF and 6-day ON cells is reminiscent of cells undergoing *trans*-differentiation. Scale bar, 15 μm.

(C) FACS-based cell cycle analysis in "inverted" cells at different time points after *CDC6* induction (±SD, n = 3).

(D) Representative images of OFF, ON, and ESC or "bypass" (bottom) cells stained with SenTraGor to assess senescence bypass in "inverted" (yellow color defined) compared with WT (red and green color defined) cells. Scale bar, 15 μm.

(E) Plots depicting mean proliferation (±SD, n = 3) in the different states of WT and "inverted" cells. Significantly different from OFF, *p < 0.05; unpaired two-tailed Student's t test.

(legend continued on next page)

BHLHE40 inversion, which occurs *in vivo* (Figure S3G) and appears to be central in the ESC phenomenon, a variant of the reciprocal translocation involving chromosomes 9 and 22 typically identified in chronic myelogenous leukemia (CML) (Valencia et al., 2009; Krishna Chandran et al., 2019), was also shared by all three ESC populations (Figure S3I). Finally, all genes localized in the remaining shared CNVs have been associated with the senescence process (for details, see Table S2B). These findings are also consistent with phase III of our hypothesis (Figure 1A).

A CRISPR-generated inversion in chr3 suffices for senescence bypass

We next tested whether genetic alterations, obtained early upon senescence entry and maintained in ESC cells, are functionally relevant to this transition. In other words, does the inversion in chr3 facilitate ESC by promoting *BHLHE40* re-induction in response to oncogenic stimuli? To answer this, we first examined BHLHE40 protein levels along a time course from OFF to ESC cells. Baseline levels in OFF cells are reduced upon *CDC6* induction but increased markedly in the ESC state (Figure S4C). Interestingly, BHLHE40 suppression was partially alleviated by day 6 (Figure S4C). This coincides with the window of error-prone DSB repair (Figure 2A) and, thus, with the presumed acquisition time of the chr3 inversion.

Next we used CRISPR-Cas9 editing in HBECs (Figure S6A) to target sequences within 72 (at 2,920,305) and 50 bp (at 6,680,932) of the inversion breakpoints mapped previously using WGS (Figures 4C and 4D). We generated two independent clones carrying this 3.7-Mbp heterozygous inversion (Figures 6A and S6Bi) and used ChIP-seq to map the binding sites of BHLHE40 genome wide. We discovered 2,576 robust peaks harboring the BHLHE40 binding motif and mostly overlapping gene promoters (Figures S6C and S6D).

Notably, ''inverted'' cells demonstrated loss of epithelial features with accentuated spindle morphology, low E-cadherin and emergent vimentin expression (Figure 6B), reminiscent of the metastable state characterizing cells undergoing *trans*-differentiation (Nieto et al., 2016). Strikingly, and in accordance with our hypothesis, upon *CDC6* induction, the clones carrying this inversion never ceased to proliferate, nor did they acquire morphological features of senescence, supporting the notion that they bypass the senescence barrier (Figures 6C, 6D, S6Bii, and S6Biii). Notably, at the initial phases of *CDC6* induction, the observed low S-phase cell percentages can be attributed to the particularly energy-demanding state of this metastable phenotype (Nieto et al., 2016) and/or to DDR activation (Figures S6Biv and S6Bv). This is nevertheless not adequate for triggering senescence in this cell context (Figures 6B–6D). Soon after this ''slow growth'' phase (Figures 6C and S6Biii), inverted cells progressively increase their growth rate and invasion capacity (Figures 6E and 6F).

Critically, both inverted clones overexpressed BHLHE40 upon *CDC6* induction (Figures 6G, 6H, and S6Bvi), and this overexpression appears to drive gene expression changes that favor senescence suppression and cell cycle re-entry (Figures 6I and S6E). Indeed, stable overexpression of *BHLHE40* in the wild-type HBEC-CDC6-TetON system led to bypass of senescence upon CDC6 activation as well (Figure 6J). Non-induced cells stably harboring high levels of BHLHE40 (Figure 6J) demonstrated a spindle-like morphology, similar to non-induced inverted cells (Figures 6B and 6D). As negative controls, CRISPR-Cas9-engineered cells that failed to acquire the desired inversion did enter senescence upon *CDC6* induction (Figure S6F). A single inversion in one of the alleles harboring *BHLHE40* suffices for driving constitutive expression of this circadian transcription factor in response to oncogenic stimulation and ESC from senescence (phase IV of the working hypothesis; Figure 1A).

Genomic instability-mediated chromatin refolding underlies BHLHE40 induction and ESC from senescence

It is now understood that changes in three-dimensional (3D) chromosome architecture, like those caused by inversions, may mechanistically explain disease manifestation, including cancer (Ibrahim and Mundlos, 2020). To test whether this can also explain *BHLHE40* upregulation, we investigated 3D reorganization in the extended *BHLHE40* locus. We used our ''inverted'' HBECs to generate high-resolution Hi-C maps from OFF and ''senescence-bypass'' cells (Table S4A). Genome-wide comparison of these data revealed that ''bypass'' cells exhibit an increase in sub-Mbp interactions (Figure 7A), accompanied by changes in the identity of compartments. Approximately 10% of A- or B-compartments switch to B or A, respectively, and this switching explains a considerable fraction (almost 50%) of the gene expression changes that underlie senescence bypass (Figure 7B). However, only marginal changes to topologically associating domain (TAD) positions (Beagan and Phillips-Cremins, 2020) were found (Figure 7C). These effects are, for the most part, the converse of what was observed for cells transitioning into senescence (Zirkel et al., 2018).

Looking specifically into the 3D organization of chromatin around the inversion region on chr3, we made three key observations. First, *BHLHE40* resides in one of the two centrally located TADs of this extended locus, whose long-range contacts do not change between OFF and ''bypass'' cells (Figure 7D). Thus, we can rule out the ''classic'' scenario of *BHLHE40* re-expression because of ectopic contacts with enhancers in adjacent TADs

(F) As in (E) but quantifying cell invasion capacity (±SD, n = 3). Significantly different from OFF, *p < 0.05; unpaired two-tailed Student's t test.
(G) Western blots showing BHLHE40 suppression upon *CDC6* induction in WT cells. GAPDH is a loading control.
(H) Left: as in (G) but showing strong BHLHE40 re-expression upon *CDC6* induction in cells carrying the CRISPR-generated inversion. Center/right: blots showing that aphidicolin (APH) treatment suppresses CDC6-driven BHLHE40 re-expression in ''inverted'' bypass cells. GAPDH is a loading control.
(I) Heatmap of gene expression data depicting inverse patterns for cell cycle and senescence regulators between 6-day *CDC6*-ON WT and bypass ''inverted'' cells.
(J) Left: western blots showing BHLHE40 overexpression ($BHLHE40^{OE}$) in transfected WT cells. GAPDH is a loading control. Right: representative images of OFF, ON, and ''bypass'' cells stained with SenTraGor to assess senescence bypass in *CDC6*-ON $BHLHE40^{OE}$ compared with WT cells. Ki-67 staining for cell proliferation was performed. α-HA, anti-hemagglutinin. Scale bar, 20 μm.

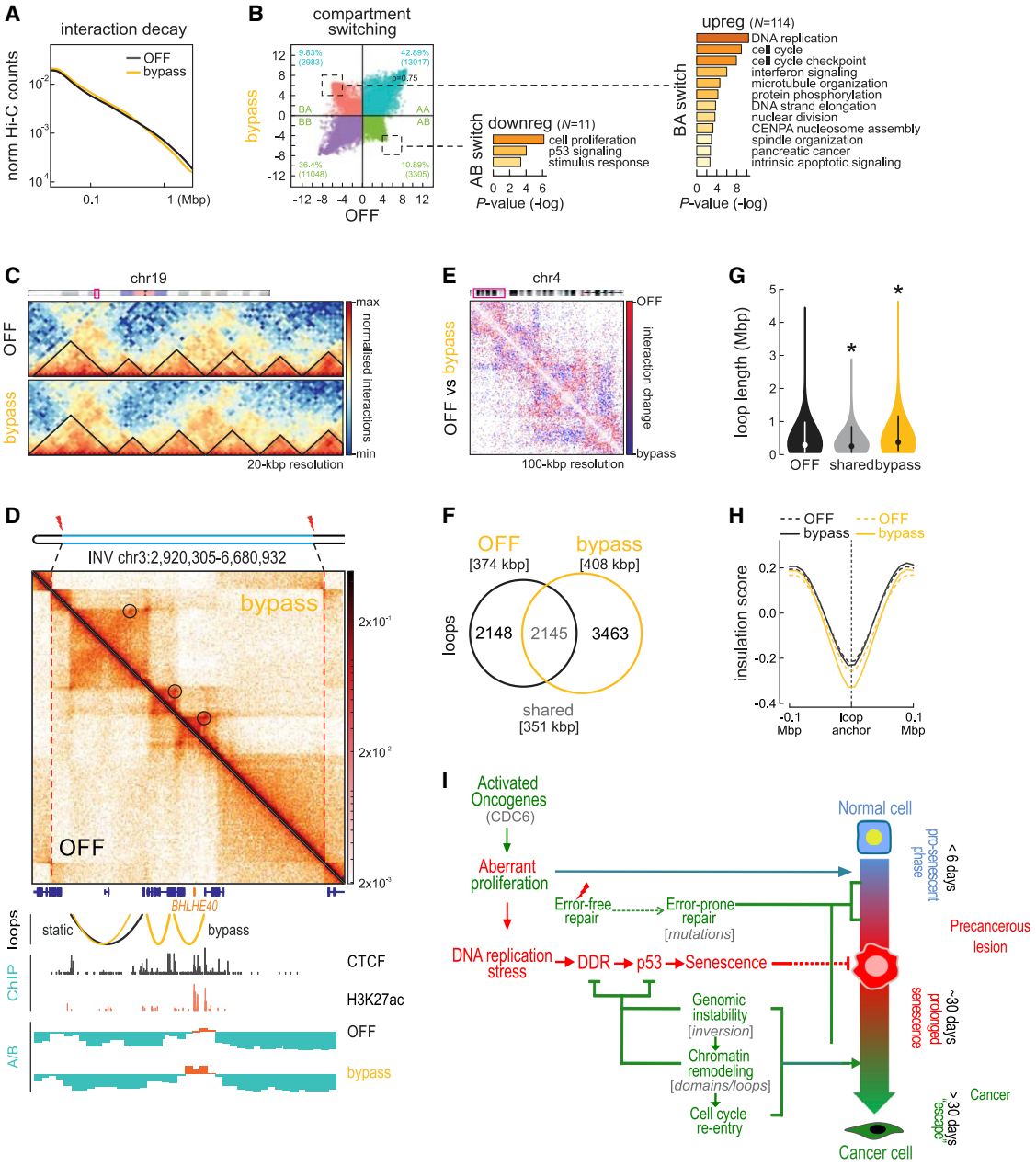

Figure 7. Analysis of spatial chromatin interactions in "inverted" OFF and bypass cells

(A) Line plot showing mean interaction strength decay (HiC counts) in relation to increasing separation of interacting fragments in OFF (black) and bypass "inverted" cells (yellow).

(B) Changes in A/B-compartments in bypass versus OFF HiC data. Strong B-to-A and A-to-B switching (dotted squares) is indicated, and the GO terms associated with differentially expressed genes embedded in each switched domain are shown.

(C) Exemplary HiC heatmaps from OFF and bypass cells showing negligible changes in TAD positions for a subregion on chr19.

(D) Composite HiC heatmap depicting interactions from OFF (bottom) and bypass "inverted" cells (top) in the region harboring *BHLHE40* on chr3. The data are aligned with CTCF and H3K27ac ChIP-seq data from normal OFF HBECs as well as with A/B-compartment positions from OFF and bypass cells. CTCF-anchored loops emerging upon senescence bypass are denoted on the HiC map (circles) and aligned below (yellow arches).

(E) Subtracted HiC heatmap showing changes in interactions upon transition from OFF to bypass "inverted" cells for a subregion on chr4.

(F) Venn diagram showing the number of loops unique to OFF and bypass "inverted" cells or shared. Median loop lengths (square brackets) are indicated.

(G) Violin plots showing distribution of lengths for the loops from (H). Significantly different from OFF, *p < 0.05; Wilcoxon-Mann-Whitney test.

(H) Line plots showing mean insulation of chromatin interactions in the 200 kbp around loop anchors unique to OFF (black) or bypass "inverted" loops (yellow) using HiC data from OFF (dotted lines) and bypass cells (solid lines).

(legend continued on next page)

(Ibrahim and Mundlos, 2020). Second, we found emergence of new loops in this 4-Mbp region that contribute to the enhanced insulation of the two central TADs from one another (Figure 7D, circles). Strikingly, a survey of this same 4-Mbp region encompassing *BHLHE40* in publicly available Hi-C data showed that these two centrally located TADs appear fused in normal tissue but well insulated in cancer cells (Figures S7A and S7B), mirroring our OFF and "bypass" data, respectively. Third, we found that strong loop emergence coincided with strengthening and broadening of the small A-compartment harboring *BHLHE40*, which is in line with its more potent activation Figure 7D, bottom).

Given these effects in the *BHLHE40* domain, we speculated that changes to CTCF loops genome-wide might explain the changes underlying senescence bypass. Indeed, subtracting OFF from "bypass" Hi-C data revealed new long-range contacts emerging (Figure 7E). Across all chromosomes, ~3,500 new loops arise, whereas ~2,150 specific to OFF cells are lost (Figure 7F). In line with our subtracted maps, bypass-specific loops are, on average, larger than OFF-specific ones (Figure 7G). Interestingly, and exactly as in the case of the *BHLHE40* domain, these bypass-specific loops arise at positions of existing insulation that become markedly strengthened. At the same time, insulation at the anchors of OFF-specific loops shows little fluctuation (Figure 7H). These types of changes suggests rewiring of regulatory gene-enhancer interactions. To cite two characteristic examples, we see emergence of bypass-specific loops in loci suppressed upon senescence bypass. In both cases, these loops trap the two genes, *RRM2* and *NCAPG* (involved in replication and mitosis, respectively), between adjacent insulated domains to mediate their downregulation (Figures S7C and S7D; Table S3). In contrast, *LAP3* finds itself within an emerging bypass-specific loop and is induced (Figure S7D).

Furthermore, given that replication origins in mammals are not defined by specific sequences but by structural chromatin context (Antequera, 2004; Cvetic and Walter, 2005), we reasoned that changes in chromatin segment orientation could additionally reorganize the replication process and, in turn, affect gene transcription (Lin et al., 2003; Chen et al., 2019; Fisher and Méchali 2003). The dependence of transcription on replication (S phase dependence) has been demonstrated in various developmental procedures (Fisher and Méchali 2003). This, combined with the fact that replication origins can be activated because of replication stress (Courtot et al., 2018), like that induced by *CDC6* overexpression (Petrakis et al., 2016; Hills and Diffley 2014), prompted us to investigate whether BHLHE40 upregulation is linked to replication. Indeed, treating bypass "inverted" cells with aphidicolin markedly reduced the protein levels of BHLHE40, which was not the case for OFF cells (Figure 6H). Likewise, wild-type ESC but not OFF cells responded in exactly the same way to aphidicolin by suppressing BHLHE40 levels (Figure S6Bvii). Such 3D reorganization events can explain gene expression changes leading to senescence bypass.

DISCUSSION

Entry into senescence is a ubiquitous physiological stress response, and it is also triggered by oncogene activation to serve as a tumor-suppressing mechanism (Gorgoulis et al., 2019). Still, as with any form of senescence, if the resulting cells are not removed from their niche in a timely manner, then an undesirable pro-tumorigenic facet can arise (Rodier and Campisi, 2011; Muñoz-Espín and Serrano, 2014; Gorgoulis et al., 2018; 2019). This adverse effect has been attributed to the SASP, the secretory cocktail senescence cells release into their surroundings to trigger chronic inflammation (Gorgoulis et al., 2019; Coppé et al., 2010). However, recent reports by us and others have documented that some cells can "escape" this state of OIS to initiate malignancy (Galanos et al., 2016; Komseli et al., 2018; Milanovic et al., 2018; Patel et al., 2016; Yu et al., 2018), but the molecular mechanisms underlying such an ESC still remain obscure.

Here we present the first mechanistic evidence of how DNA lesions acquired early upon entry into OIS can drive this phenomenon of ESC. We exploit normal HBECs driven to senescence by overexpressing the *CDC6* oncogene. From the populations of these senescent cells, mesenchymal-like, aggressively proliferating cells eventually emerge within ~30 days. Thus, we can essentially mimic "cancer evolution" to find that (1) forced *CDC6* expression induces DSBs genome wide as early as 3 days of senescence entry; (2) these DSBs are repaired predominantly in an error-prone manner; and (3) misrepaired lesions are actively selected during this "cancer evolution" time course and appear to be essential for establishment and/or maintenance of the ESC clones (Figure 7I).

Large genomic cancer studies have shown that the path to malignancy is not uniquely defined but needs to fulfill particular milestones that allow the aggressive and unhindered proliferation capacity of cancer cells (Gorgoulis et al., 2018). We propose that this also applies to ESC from senescence. Indeed, our independent ESC clones display recurrent structural and sequence variants that are linked to their phenotype; for example, precise recapitulation of frequent cancer mutations in *MUC16* and *NEB* or the resemblance of the ESC SNV signature to that discovered previously in tumors in affected individuals (Alexandrov et al., 2013). Another prerequisite for HBEC ESC and for most examples of malignant transformation (Aylon and Oren, 2011) is inactivation of the p53 response (Halazonetis et al., 2008). This also seems to occur in our model—not via *CDC6*-dependent mutation of the *TP53* locus itself but indirectly via MDM2 upregulation to disable p53. This course of events is not confined to the bronchial epithelium but can be recapitulated in human pancreatic duct epithelial cells (HPDECs) that carry an inducible *CDC6* construct and in which p53 function is inactivated via HPV16-E6 transduction (Ouyang et al., 2000). This is a relevant cell system because *CDC6* overexpression and senescence are frequently detected in precancerous pancreatic lesions

(I) Update of the DNA damage model for cancer development (Halazonetis et al., 2008). Cells respond to oncogenic stimuli by eliciting senescence as an anti-tumor barrier. The high DNA damage (DSBs) burden amassing during senescence engages error-prone repair mechanisms. Consequently, genetic aberrations accumulate with concurrent chromatin remodeling that provide a "pool" of genomic defects from which those that facilitate ESC from senescence, cell cycle re-entry, and aggressive features are selected and maintained.

(Myrianthopoulos et al., 2019). As predicted, following *CDC6* induction, HPDECs follow a trajectory that bypasses senescence (Figure S4F).

A prominent and recurrent feature in our ESC clones is the 3.7-Mbp heterozygous inversion on chr3. Although essentially all types of structural aberrations have been functionally linked to cancer development (Stratton et al., 2009; Danieli and Papantonis, 2020), inversions confer particular properties regarding their selection. Their predominantly heterozygous nature allows lower recombination rates and, thus, selective maintenance so that the affected genes operate in an advantageous "enhanced" mode (Puig et al., 2015; Wellenreuther and Bernatchez, 2018). Accordingly, the *BHLHE40* gene harbored in our 3.7-Mbp inversion encodes a circadian transcription factor known for controlling a large number of human genes and a variety of processes, including the cell cycle (Hunt and Sassone-Corsi, 2007; Wood et al., 2009; Kato et al., 2014; Sato et al., 2016). In our system, control of key differentially regulated genes in ESC cells can be attributed to BHLHE40. Despite the fact that its expression has been linked to senescence (Collado et al., 2005; Qian et al., 2008), dependence of this ESC phenomenon on BHLHE40 can be explained by the following sequence of molecular events. Soon after senescence induction, between a 3- and 6-day time window, erroneous DNA repair establishes an inverted locus where this circadian gene is now responsive to *CDC6* overexpression and upregulated markedly. A major factor in this process appears to be CTCF and its ability to direct loop formation along chromosomes (Rada-Iglesias et al., 2018; Braccioli and de Wit, 2019). Remodeling of the *BHLHE40* topological domain via emergence of *de novo* loops coincides with its activation. The resulting abundance of this potent transcription factor is reminiscent of an oncogenic stimulus that can only exert its pro-tumorigenic potential when relieved of the senescence barrier. Such a mode of action would then explain contentious reports showing that BHLHE40 triggers senescence or supports cell proliferation, EMT, tumor formation, and poor survival (Sato et al., 2016; Yamada and Miyamoto, 2005; Qian et al., 2008). It can also explain ESC-relevant gene expression changes that correlate with loop rewiring, in line with the proposed role of BHLHE40 in regulating CTCF binding genome wide (Hu et al., 2020).

Our work suggests that it is in the early phase of OIS that the "genetic seeds" of the forthcoming malignant transformation are "planted" in chromosomes (Figure 7I). Whether ESC will always be the inevitable destiny of a subset of cells or whether there are cell-autonomous or non-cell-autonomous factors that can dictate this fate remains to be elucidated. The prospect that senescent cells can escape from their non-proliferative state may have far-reaching implications. Hence, targeting senescent cells can be of major clinical importance by eliminating a potential source of recurrence. In light of the expanding field of senotherapeutics (Zhu et al., 2015; Childs et al., 2015; Gorgoulis et al., 2019; Myrianthopoulos et al., 2019), this may inspire future therapeutic choices.

Limitations of the study

Our study provides evidence that OIS is a time window during which DNA lesions repaired poorly because of replication stress are seeded throughout the genome. Some of these are further selected because they allow a subset of cells to "escape" senescence and re-enter cell cycle progression. Particularly, we identified *BHLHE40*, a circadian rhythm gene, as a key driver of cell cycle re-entry and malignant transformation of originally senescent cells. *BHLHE40* activation is a result of a large inversion harboring its locus. However, it remains unclear whether the chromatin refolding changes we recorded upon its induction are causal or the readout of gene activation. Moreover, we cannot rule out the possibility that escape from senescence can also occur independent of such a genomic inversion and via some other mechanism, which would still likely involve *BHLHE40* activation. Finally, although our data suggest that BHLHE40 is an effector linking replication coordination with circadian rhythms, further work is warranted to understand the underlying mechanisms.

STAR★METHODS

Detailed methods are provided in the online version of this paper and include the following:

- KEY RESOURCES TABLE
- RESOURCE AVAILABILITY
  - Lead contact
  - Materials availability
  - Data and code availability
- EXPERIMENTAL MODEL AND SUBJECT DETAILS
- METHOD DETAILS
  - Plasmid generation
  - siRNA and plasmid transfections
  - Selection of escaped clones
  - Protein extraction, cell fractionation and immunoblot analysis
  - Immunofluorescence analysis
  - Immunocytochemistry
  - Cell growth analysis
  - 3D (organotypic) culture
  - Senescence detection with SenTraGor
  - Invasion assay
  - Tumorigenicity assay
  - Flow cytometry analysis (FACS) - Cell Cycle analysis
  - 5′-EU incorporation based nascent RNA assay
  - QIBC analysis
  - DR-GFP, SA-GFP and BIR-GFP reporter assays
  - DNA fiber fluorography (combing assay)
  - Breaks Labeling *In Situ* and Sequencing (BLISS)
  - Next Generation Sequencing and Bioinformatics analysis
  - RNA isolation, sequencing, and data analysis
  - Chromatin immunoprecipitation (ChIP), sequencing, and data analysis
  - Genome-wide chromosome conformation capture (Hi-C) and data analysis
  - CRISPR/Cas9 inversion generation
  - Sanger sequencing
  - Survival data analysis
- QUANTIFICATION AND STATISTICAL ANALYSIS

SUPPLEMENTAL INFORMATION

Supplemental information can be found online at https://doi.org/10.1016/j.molcel.2021.10.017.

ACKNOWLEDGMENTS

We would like to thank Dr. Panagiota Kafasla for technical support. We are also thankful to Dr. Claudia and Jiri Lukas for providing an additional antibody against RAD52 for better representation of focus formation. V.G.G. and C.P.Z. are financially supported by the European Union Horizon 2020 Research and Innovation Program under Marie Sklodowska-Curie grant agreement 722729 (SYNTRAIN). V.G.G. is also supported by the National Public Investment Program of the Ministry of Development and Investment/General Secretariat for Research and Technology in the framework of the Flagship Initiative to address SARS-CoV-2 (2020ΣΕ01300001); the Welfare Foundation for Social & Cultural Sciences (KIKPE), Athens, Greece; a H. Pappas donation; grants 775 (Hippo) and 3782 (PACOREL) from the Hellenic Foundation for Research and Innovation (HFRI); and NKUA-SARG grant 70/3/8916. This work is also co-financed by Greece and the European Union (European Social Fund [ESF]) through the Operational Program "Human Resources Development, Education and Lifelong Learning" in the context of the project "Reinforcement of Postdoctoral Researchers—2nd Cycle" (MIS-5033021), implemented by the State Scholarships Foundation (IKY). A.P. is supported by the Deutsche Forschungsgemeinschaft via the Clinical Research Unit KFO5002 project grant (CO 1568/2-1) and the Priority Program SPP2202 (grant PA 2456/11-1). Y.Z. is also supported by the IMPRS "Molecular Biology" Program (GGNB), part of the Göttingen Graduate Center for Neurosciences, Biophysics and Molecular Biosciences (GGNB). P.G. is supported by the Danish Cancer Society (R167-A11068) and the Lundbeck Foundation (R322-2019-2577). Z.G. is supported by the Novo Nordisk Foundation (0052647), and D.H.L. is supported by the Independent Research Fund Denmark (8045-00057A) and the Danish Cancer Society. J.B. and his team were supported by the Danish Cancer Society (R204-A12617-B153), the Novo Nordisk Foundation (16854), the Danish National Research Foundation (Project CARD, DNRF 125), the Swedish Research Council (VR-MH 2014-46602-117891-30) and the Cancerfonden (170176).

AUTHOR CONTRIBUTIONS

C.P.Z., P.G., A.A., I.M., N.L., and K.E., cell culture and manipulation, immunoblots, FACS, immunofluorescence analysis, immunocytochemistry, SenTraGor staining, PCR, and 3D cell culture; P.G. and Z.G., QIBC analysis; C.P.Z., invasion and tumorigenicity assays; C.P.Z., P.G., and A.M.-M., combing assays; A.A., Y.Z., A.M., E.G.G., and K.S., ChIP-seq, Hi-C, CRISPR-Cas9 editing, and RNA-seq; D.E.P., EU assay; R.M., S.G., and N.C., BLISS; A.K., T.K., Y.Z., E.G.G., A.T., A. Polyzos, and A. Polyzou, bioinformatics analyses; A. Papaspyrpoulos, A.K., T.K., A.T., and A. Polyzou, survival analyses; C.P.Z., P.G., A.A., A.K., A. Papaspyrpoulos, D.H.L., M.D., K.E., J.B., A. Papantonis, and V.G.G., data analysis and interpretation and manuscript preparation; P.G., J.B., A. Papantonis, and V.G.G., experimental design, supervision and project funding, and manuscript writing with input from all co-authors.

DECLARATION OF INTERESTS

The authors declare no competing interests.

Received: January 14, 2021
Revised: July 14, 2021
Accepted: October 16, 2021
Published: November 17, 2021

REFERENCES

Abdennur, N., and Mirny, L.A. (2020). Cooler: scalable storage for Hi-C data and other genomically labeled arrays. Bioinformatics *36*, 311–316.

Alexandrov, L.B., Nik-Zainal, S., Wedge, D.C., Aparicio, S.A., Behjati, S., Biankin, A.V., Bignell, G.R., Bolli, N., Borg, A., Børresen-Dale, A.L., et al.; Australian Pancreatic Cancer Genome Initiative; ICGC Breast Cancer Consortium; ICGC MMML-Seq Consortium; ICGC PedBrain (2013). Signatures of mutational processes in human cancer. Nature *500*, 415–421.

Anders, S., and Huber, W. (2010). Differential expression analysis for sequence count data. Genome Biol. *11*, R106.

Anders, S., Pyl, P.T., and Huber, W. (2015). HTSeq–a Python framework to work with high-throughput sequencing data. Bioinformatics *31*, 166–169.

Antequera, F. (2004). Genomic specification and epigenetic regulation of eukaryotic DNA replication origins. EMBO J. *23*, 4365–4370.

Aylon, Y., and Oren, M. (2011). New plays in the p53 theater. Curr. Opin. Genet. Dev. *21*, 86–92.

Bartkova, J., Rezaei, N., Liontos, M., Karakaidos, P., Kletsas, D., Issaeva, N., Vassiliou, L.V., Kolettas, E., Niforou, K., Zoumpourlis, V.C., et al. (2006). Oncogene-induced senescence is part of the tumorigenesis barrier imposed by DNA damage checkpoints. Nature *444*, 633–637.

Beagan, J.A., and Phillips-Cremins, J.E. (2020). On the existence and functionality of topologically associating domains. Nat. Genet. *52*, 8–16.

Bouwman, B.A.M., Agostini, F., Garnerone, S., Petrosino, G., Gothe, H.J., Sayols, S., Moor, A.E., Itzkovitz, S., Bienko, M., Roukos, V., and Crosetto, N. (2020). Genome-wide detection of DNA double-strand breaks by in-suspension BLISS. Nat. Protoc. *15*, 3894–3941.

Braccioli, L., and de Wit, E. (2019). CTCF: a Swiss-army knife for genome organization and transcription regulation. Essays Biochem. *63*, 157–165.

Braig, M., Lee, S., Loddenkemper, C., Rudolph, C., Peters, A.H.F.M., Schlegelberger, B., Stein, H., Dörken, B., Jenuwein, T., and Schmitt, C.A. (2005). Oncogene-induced senescence as an initial barrier in lymphoma development. Nature *436*, 660–665.

Chambers, S.M., Boles, N.C., Lin, K.-Y.K., Tierney, M.P., Bowman, T.V., Bradfute, S.B., Chen, A.J., Merchant, A.A., Sirin, O., Weksberg, D.C., et al. (2007). Hematopoietic fingerprints: an expression database of stem cells and their progeny. Cell Stem Cell *1*, 578–591.

Chen, Z., Trotman, L.C., Shaffer, D., Lin, H.K., Dotan, Z.A., Niki, M., Koutcher, J.A., Scher, H.I., Ludwig, T., Gerald, W., et al. (2005). Crucial role of p53-dependent cellular senescence in suppression of Pten-deficient tumorigenesis. Nature *436*, 725–730.

Chen, X., Schulz-Trieglaff, O., Shaw, R., Barnes, B., Schlesinger, F., Källberg, M., Cox, A.J., Kruglyak, S., and Saunders, C.T. (2016). Manta: rapid detection of structural variants and indels for germline and cancer sequencing applications. Bioinformatics *32*, 1220–1222.

Chen, Y.H., Keegan, S., Kahli, M., Tonzi, P., Fenyö, D., Huang, T.T., and Smith, D.J. (2019). Transcription shapes DNA replication initiation and termination in human cells. Nat. Struct. Mol. Biol. *26*, 67–77.

Childs, B.G., Durik, M., Baker, D.J., and van Deursen, J.M. (2015). Cellular senescence in aging and age-related disease: from mechanisms to therapy. Nat. Med. *21*, 1424–1435.

Chugh, S., Gnanapragassam, V.S., Jain, M., Rachagani, S., Ponnusamy, M.P., and Batra, S.K. (2015). Pathobiological implications of mucin glycans in cancer: Sweet poison and novel targets. Biochim. Biophys. Acta *1856*, 211–225.

Collado, M., Gil, J., Efeyan, A., Guerra, C., Schuhmacher, A.J., Barradas, M., Benguría, A., Zaballos, A., Flores, J.M., Barbacid, M., et al. (2005). Tumour biology: senescence in premalignant tumours. Nature *436*, 642.

Coppé, J.P., Desprez, P.Y., Krtolica, A., and Campisi, J. (2010). The senescence-associated secretory phenotype: the dark side of tumor suppression. Annu. Rev. Pathol. *5*, 99–118.

Courtot, L., Hoffmann, J.S., and Bergoglio, V. (2018). The protective role of dormant origins in response to replicative stress. Int. J. Mol. Sci. *19*, 3569.

Cvetic, C., and Walter, J.C. (2005). Eukaryotic origins of DNA replication: could you please be more specific? Semin. Cell Dev. Biol. *16*, 343–353.

Danieli, A., and Papantonis, A. (2020). Spatial genome architecture and the emergence of malignancy. Hum. Mol. Genet. *29* (R2), R197–R204.

Di Micco, R., Fumagalli, M., Cicalese, A., Piccinin, S., Gasparini, P., Luise, C., Schurra, C., Garre', M., Nuciforo, P.G., Bensimon, A., et al. (2006). Oncogene-induced senescence is a DNA damage response triggered by DNA hyper-replication. Nature *444*, 638–642.

Dobin, A., Davis, C.A., Schlesinger, F., Drenkow, J., Zaleski, C., Jha, S., Batut, P., Chaisson, M., and Gingeras, T.R. (2013). STAR: ultrafast universal RNA-seq aligner. Bioinformatics *29*, 15–21.

Evangelou, K., Lougiakis, N., Rizou, S.V., Kotsinas, A., Kletsas, D., Muñoz-Espín, D., Kastrinakis, N.G., Pouli, N., Marakos, P., Townsend, P., et al. (2017). Robust, universal biomarker assay to detect senescent cells in biological specimens. Aging Cell *16*, 192–197.

Fisher, D., and Méchali, M. (2003). Vertebrate HoxB gene expression requires DNA replication. EMBO J. *22*, 3737–3748.

Ford, E., Nikopoulou, C., Kokkalis, A., and Thanos, D. (2014). A method for generating highly multiplexed ChIP-seq libraries. BMC Res. Notes *7*, 312.

Furukawa, T., Duguid, W.P., Rosenberg, L., Viallet, J., Galloway, D.A., and Tsao, M.S. (1996). Long-term culture and immortalization of epithelial cells from normal adult human pancreatic ducts transfected by the E6E7 gene of human papilloma virus 16. Am. J. Pathol. *148*, 1763–1770.

Galanos, P., Vougas, K., Walter, D., Polyzos, A., Maya-Mendoza, A., Haagensen, E.J., Kokkalis, A., Roumelioti, F.M., Gagos, S., Tzetis, M., et al. (2016). Chronic p53-independent p21 expression causes genomic instability by deregulating replication licensing. Nat. Cell Biol. *18*, 777–789.

Galanos, P., Pappas, G., Polyzos, A., Kotsinas, A., Svolaki, I., Giakoumakis, N.N., Glytsou, C., Pateras, I.S., Swain, U., Souliotis, V.L., et al. (2018). Mutational signatures reveal the role of RAD52 in p53-independent p21-driven genomic instability. Genome Biol. *19*, 37.

Gery, S., Komatsu, N., Baldjyan, L., Yu, A., Koo, D., and Koeffler, H.P. (2006). The circadian gene per1 plays an important role in cell growth and DNA damage control in human cancer cells. Mol. Cell *22*, 375–382.

Goodspeed, A., Heiser, L.M., Gray, J.W., and Costello, J.C. (2016). Tumor-Derived Cell Lines as Molecular Models of Cancer Pharmacogenomics. Mol. Cancer Res. *14*, 3–13.

Gorgoulis, V.G., Pefani, D.E., Pateras, I.S., and Trougakos, I.P. (2018). Integrating the DNA damage and protein stress responses during cancer development and treatment. J. Pathol. *246*, 12–40.

Gorgoulis, V., Adams, P.D., Alimonti, A., Bennett, D.C., Bischof, O., Bishop, C., Campisi, J., Collado, M., Evangelou, K., Ferbeyre, G., et al. (2019). Cellular senescence: defining a path forward. Cell *179*, 813–827.

Gothe, H.J., Bouwman, B.A.M., Gusmao, E.G., Piccinno, R., Petrosino, G., Sayols, S., Drechsel, O., Minneker, V., Josipovic, N., Mizi, A., et al. (2019). Spatial chromosome folding and active transcription drive DNA fragility and formation of oncogenic MLL translocations. Mol. Cell *75*, 267–283.e12.

Halazonetis, T.D., Gorgoulis, V.G., and Bartek, J. (2008). An oncogene-induced DNA damage model for cancer development. Science *319*, 1352–1355.

Hernandez-Segura, A., de Jong, T.V., Melov, S., Guryev, V., Campisi, J., and Demaria, M. (2017). Unmasking transcriptional heterogeneity in senescent cells. Curr. Biol. *27*, 2652–2660.e4.

Hills, S.A., and Diffley, J.F. (2014). DNA replication and oncogene-induced replicative stress. Curr. Biol. *24*, R435–R444.

Hu, G., Dong, X., Gong, S., Song, Y., Hutchins, A.P., and Yao, H. (2020). Systematic screening of CTCF binding partners identifies that BHLHE40 regulates CTCF genome-wide distribution and long-range chromatin interactions. Nucleic Acids Res. *48*, 9606–9620.

Hunt, T., and Sassone-Corsi, P. (2007). Riding tandem: circadian clocks and the cell cycle. Cell *129*, 461–464.

Ibrahim, D.M., and Mundlos, S. (2020). Three-dimensional chromatin in disease: What holds us together and what drives us apart? Curr. Opin. Cell Biol. *64*, 1–9.

Ivanova, N.B., Dimos, J.T., Schaniel, C., Hackney, J.A., Moore, K.A., and Lemischka, I.R. (2002). A stem cell molecular signature. Science *298*, 601–604.

Karakaidos, P., Taraviras, S., Vassiliou, L.V., Zacharatos, P., Kastrinakis, N.G., Kougiou, D., Kouloukoussa, M., Nishitani, H., Papavassiliou, A.G., Lygerou, Z., and Gorgoulis, V.G. (2004). Overexpression of the replication licensing regulators hCdt1 and hCdc6 characterizes a subset of non-small-cell lung carcinomas: synergistic effect with mutant p53 on tumor growth and chromosomal instability–evidence of E2F-1 transcriptional control over hCdt1. Am. J. Pathol. *165*, 1351–1365.

Kato, Y., Kawamoto, T., Fujimoto, K., and Noshiro, M. (2014). DEC1/STRA13/SHARP2 and DEC2/SHARP1 coordinate physiological processes, including circadian rhythms in response to environmental stimuli. Curr. Top. Dev. Biol. *110*, 339–372.

Kerpedjiev, P., Abdennur, N., Lekschas, F., McCallum, C., Dinkla, K., Strobelt, H., Luber, J.M., Ouellette, S.B., Azhir, A., Kumar, N., et al. (2018). HiGlass: web-based visual exploration and analysis of genome interaction maps. Genome Biol. *19*, 125.

Kim, J., Woo, A.J., Chu, J., Snow, J.W., Fujiwara, Y., Kim, C.G., Cantor, A.B., and Orkin, S.H. (2010). A Myc network accounts for similarities between embryonic stem and cancer cell transcription programs. Cell *143*, 313–324.

Knight, P.A., and Ruiz, D. (2013). A fast algorithm for matrix balancing. IMA J. Numer. Anal. *33*, 1029–1047.

Kohli, J., Wang, B., Brandenburg, S.M., Basisty, N., Evangelou, K., Varela-Eirin, M., Campisi, J., Schilling, B., Gorgoulis, V., and Demaria, M. (2021). Algorithmic assessment of cellular senescence in experimental and clinical specimens. Nat. Protoc. *16*, 2471–2498.

Komseli, E.S., Pateras, I.S., Krejsgaard, T., Stawiski, K., Rizou, S.V., Polyzos, A., Roumelioti, F.M., Chiourea, M., Mourkioti, I., Paparouna, E., et al. (2018). A prototypical non-malignant epithelial model to study genome dynamics and concurrently monitor micro-RNAs and proteins in situ during oncogene-induced senescence. BMC Genomics *19*, 37.

Krishna Chandran, R., Geetha, N., Sakthivel, K.M., Suresh Kumar, R., Jagathnath Krishna, K.M.N., and Sreedharan, H. (2019). Impact of Additional Chromosomal Aberrations on the Disease Progression of Chronic Myelogenous Leukemia. Front. Oncol. *9*, 88–99.

Kufe, D.W. (2009). Mucins in cancer: function, prognosis and therapy. Nat. Rev. Cancer *9*, 874–885.

Lagopati, N., Kotsinas, A., Veroutis, D., Evangelou, K., Papaspyropoulos, A., Arfanis, M., Falaras, P., Kitsiou, P.V., Pateras, I., Bergonzini, A., et al. (2021). Biological Effect of Silver-modified Nanostructured Titanium Dioxide in Cancer. Cancer Genomics Proteomics *18* (3, Suppl), 425–439.

Langmead, B., and Salzberg, S.L. (2012). Fast gapped-read alignment with Bowtie 2. Nat. Methods *9*, 357–359.

Li, H., and Durbin, R. (2010). Fast and accurate long-read alignment with Burrows-Wheeler transform. Bioinformatics *26*, 589–595.

Li, H., Handsaker, B., Wysoker, A., Fennell, T., Ruan, J., Homer, N., Marth, G., Abecasis, G., and Durbin, R.; 1000 Genome Project Data Processing Subgroup (2009). The sequence alignment/map format and SAMtools. Bioinformatics *25*, 2078–2079.

Lin, C.M., Fu, H., Martinovsky, M., Bouhassira, E., and Aladjem, M.I. (2003). Dynamic alterations of replication timing in mammalian cells. Curr. Biol. *13*, 1019–1028.

Liontos, M., Koutsami, M., Sideridou, M., Evangelou, K., Kletsas, D., Levy, B., Kotsinas, A., Nahum, O., Zoumpourlis, V., Kouloukoussa, M., et al. (2007). Deregulated overexpression of hCdt1 and hCdc6 promotes malignant behavior. Cancer Res. *67*, 10899–10909.

Masri, S., Cervantes, M., and Sassone-Corsi, P. (2013). The circadian clock and cell cycle: interconnected biological circuits. Curr. Opin. Cell Biol. *25*, 730–734.

Mazzoccoli, G., Castellana, S., Carella, M., Palumbo, O., Tiberio, C., Fusilli, C., Capocefalo, D., Biagini, T., Mazza, T., and Lo Muzio, L. (2017). A primary tumor gene expression signature identifies a crucial role played by tumor stroma myofibroblasts in lymph node involvement in oral squamous cell carcinoma. Oncotarget *8*, 104913–104927.

Michaloglou, C., Vredeveld, L.C., Soengas, M.S., Denoyelle, C., Kuilman, T., van der Horst, C.M., Majoor, D.M., Shay, J.W., Mooi, W.J., and Peeper, D.S. (2005). BRAFE600-associated senescence-like cell cycle arrest of human naevi. Nature *436*, 720–724.

Milanovic, M., Fan, D.N.Y., Belenki, D., Däbritz, J.H.M., Zhao, Z., Yu, Y., Dörr, J.R., Dimitrova, L., Lenze, D., Monteiro Barbosa, I.A., et al. (2018). Senescence-associated reprogramming promotes cancer stemness. Nature *553*, 96–100.

Moreno, A., Carrington, J.T., Albergante, L., Al Mamun, M., Haagensen, E.J., Komseli, E.S., Gorgoulis, V.G., Newman, T.J., and Blow, J.J. (2016). Unreplicated DNA remaining from unperturbed S phases passes through mitosis for resolution in daughter cells. Proc. Natl. Acad. Sci. USA *113*, E5757–E5764.

Muñoz-Espín, D., and Serrano, M. (2014). Cellular senescence: from physiology to pathology. Nat. Rev. Mol. Cell Biol. *15*, 482–496.

Myrianthopoulos, V., Evangelou, K., Vasileiou, P.V.S., Cooks, T., Vassilakopoulos, T.P., Pangalis, G.A., Kouloukoussa, M., Kittas, C., Georgakilas, A.G., and Gorgoulis, V.G. (2019). Senescence and senotherapeutics: a new field in cancer therapy. Pharmacol. Ther. *193*, 31–49.

Nagy, Á., Lánczky, A., Menyhárt, O., and Győrffy, B. (2018). Validation of miRNA prognostic power in hepatocellular carcinoma using expression data of independent datasets. Sci. Rep. *8*, 9227.

Negrini, S., Gorgoulis, V.G., and Halazonetis, T.D. (2010). Genomic instability–an evolving hallmark of cancer. Nat. Rev. Mol. Cell Biol. *11*, 220–228.

Nieto, M.A., Huang, R.Y., Jackson, R.A., and Thiery, J.P. (2016). EMT: 2016. Cell *166*, 21–45.

Ochs, F., Somyajit, K., Altmeyer, M., Rask, M.B., Lukas, J., and Lukas, C. (2016). 53BP1 fosters fidelity of homology-directed DNA repair. Nat. Struct. Mol. Biol. *23*, 714–721.

Ouyang, H., Mou, Lj., Luk, C., Liu, N., Karaskova, J., Squire, J., and Tsao, M.S. (2000). Immortal human pancreatic duct epithelial cell lines with near normal genotype and phenotype. Am. J. Pathol. *157*, 1623–1631.

Patel, P.L., Suram, A., Mirani, N., Bischof, O., and Herbig, U. (2016). Derepression of hTERT gene expression promotes escape from oncogene-induced cellular senescence. Proc. Natl. Acad. Sci. USA *113*, E5024–E5033.

Pertea, M., Shumate, A., Pertea, G., Varabyou, A., Breitwieser, F.P., Chang, Y.C., Madugundu, A.K., Pandey, A., and Salzberg, S.L. (2018). CHESS: a new human gene catalog curated from thousands of large-scale RNA sequencing experiments reveals extensive transcriptional noise. Genome Biol. *19*, 208.

Petrakis, T.G., Komseli, E.S., Papaioannou, M., Vougas, K., Polyzos, A., Myrianthopoulos, V., Mikros, E., Trougakos, I.P., Thanos, D., Branzei, D., et al. (2016). Exploring and exploiting the systemic effects of deregulated replication licensing. Semin. Cancer Biol. *37-38*, 3–15.

Puig, M., Casillas, S., Villatoro, S., and Cáceres, M. (2015). Human inversions and their functional consequences. Brief. Funct. Genomics *14*, 369–379.

Qian, Y., Zhang, J., Yan, B., and Chen, X. (2008). DEC1, a basic helix-loop-helix transcription factor and a novel target gene of the p53 family, mediates p53-dependent premature senescence. J. Biol. Chem. *283*, 2896–2905.

Rada-Iglesias, A., Grosveld, F.G., and Papantonis, A. (2018). Forces driving the three-dimensional folding of eukaryotic genomes. Mol. Syst. Biol. *14*, e8214.

Ramirez, R.D., Herbert, B.S., Vaughan, M.B., Zou, Y., Gandia, K., Morales, C.P., Wright, W.E., and Shay, J.W. (2003). Bypass of telomere-dependent replicative senescence (M1) upon overexpression of Cdk4 in normal human epithelial cells. Oncogene *22*, 433–444.

Ramírez, F., Bhardwaj, V., Arrigoni, L., Lam, K.C., Grüning, B.A., Villaveces, J., Habermann, B., Akhtar, A., and Manke, T. (2018). High-resolution TADs reveal DNA sequences underlying genome organization in flies. Nat. Commun. *9*, 189.

Rao, S.S., Huntley, M.H., Durand, N.C., Stamenova, E.K., Bochkov, I.D., Robinson, J.T., Sanborn, A.L., Machol, I., Omer, A.D., Lander, E.S., and Aiden, E.L. (2014). A 3D map of the human genome at kilobase resolution reveals principles of chromatin looping. Cell *159*, 1665–1680.

Risso, D., Ngai, J., Speed, T.P., and Dudoit, S. (2014). Normalization of RNA-seq data using factor analysis of control genes or samples. Nat. Biotechnol. *32*, 896–902.

Ritschka, B., Storer, M., Mas, A., Heinzmann, F., Ortells, M.C., Morton, J.P., Sansom, O.J., Zender, L., and Keyes, W.M. (2017). The senescence-associated secretory phenotype induces cellular plasticity and tissue regeneration. Genes Dev. *31*, 172–183.

Rodier, F., and Campisi, J. (2011). Four faces of cellular senescence. J. Cell Biol. *192*, 547–556.

Rouillard, A.D., Gundersen, G.W., Fernandez, N.F., Wang, Z., Monteiro, C.D., McDermott, M.G., and Ma'ayan, A. (2016). The harmonizome: a collection of processed datasets gathered to serve and mine knowledge about genes and proteins. Database (Oxford) *2016*, baw100.

Sato, M., Vaughan, M.B., Girard, L., Peyton, M., Lee, W., Shames, D.S., Ramirez, R.D., Sunaga, N., Gazdar, A.F., Shay, J.W., and Minna, J.D. (2006). Multiple oncogenic changes (K-RAS(V12), p53 knockdown, mutant EGFRs, p16 bypass, telomerase) are not sufficient to confer a full malignant phenotype on human bronchial epithelial cells. Cancer Res. *66*, 2116–2128.

Sato, F., Bhawal, U.K., Yoshimura, T., and Muragaki, Y. (2016). DEC1 and DEC2 crosstalk between circadian rhythm and tumor progression. J. Cancer *7*, 153–159.

Sideridou, M., Zakopoulou, R., Evangelou, K., Liontos, M., Kotsinas, A., Rampakakis, E., Gagos, S., Kahata, K., Grabusic, K., Gkouskou, K., et al. (2011). Cdc6 expression represses E-cadherin transcription and activates adjacent replication origins. J. Cell Biol. *195*, 1123–1140.

Sotiriou, S.K., Kamileri, I., Lugli, N., Evangelou, K., Da-Ré, C., Huber, F., Padayachy, L., Tardy, S., Nicati, N.L., Barriot, S., et al. (2016). Mammalian RAD52 functions in break-induced replication repair of collapsed DNA replication forks. Mol. Cell *64*, 1127–1134.

Stark, J.M., Pierce, A.J., Oh, J., Pastink, A., and Jasin, M. (2004). Genetic steps of mammalian homologous repair with distinct mutagenic consequences. Mol. Cell. Biol. *24*, 9305–9316.

Stratton, M.R., Campbell, P.J., and Futreal, P.A. (2009). The cancer genome. Nature *458*, 719–724.

Thiery, J.P., Acloque, H., Huang, R.Y., and Nieto, M.A. (2009). Epithelial-mesenchymal transitions in development and disease. Cell *139*, 871–890.

Tsantoulis, P.K., Kotsinas, A., Sfikakis, P.P., Evangelou, K., Sideridou, M., Levy, B., Mo, L., Kittas, C., Wu, X.R., Papavassiliou, A.G., and Gorgoulis, V.G. (2008). Oncogene-induced replication stress preferentially targets common fragile sites in preneoplastic lesions. A genome-wide study. Oncogene *27*, 3256–3264.

Valencia, A., Cervera, J., Such, E., Barragán, E., Bolufer, P., Fuster, O., Collado, R., Martínez, J., and Sanz, M.A. (2009). Complex Variant t(9;22) Chromosome Translocations in Five Cases of Chronic Myeloid Leukemia. Adv. Hematol. *2009*, 187125.

Van der Auwera, G.A., Carneiro, M.O., Hartl, C., Poplin, R., Del Angel, G., Levy-Moonshine, A., Jordan, T., Shakir, K., Roazen, D., Thibault, J., et al. (2013). From FastQ data to high confidence variant calls: the Genome Analysis Toolkit best practices pipeline. Curr. Protoc. Bioinformatics *43*, 10.1, 33.

Wang, K., Li, M., and Hakonarson, H. (2010). ANNOVAR: functional annotation of genetic variants from high-throughput sequencing data. Nucleic Acids Res. *38*, e164.

Wellenreuther, M., and Bernatchez, L. (2018). Eco-evolutionary genomics of chromosomal inversions. Trends Ecol. Evol. *33*, 427–440.

Wong, D.J., Liu, H., Ridky, T.W., Cassarino, D., Segal, E., and Chang, H.Y. (2008). Module map of stem cell genes guides creation of epithelial cancer stem cells. Cell Stem Cell *2*, 333–344.

Wood, P.A., Yang, X., and Hrushesky, W.J. (2009). Clock genes and cancer. Integr. Cancer Ther. *8*, 303–308.

Wu, Y., Kantake, N., Sugiyama, T., and Kowalczykowski, S.C. (2008). Rad51 protein controls Rad52-mediated DNA annealing. J. Biol. Chem. *283*, 14883–14892.

Yamada, K., and Miyamoto, K. (2005). Basic helix-loop-helix transcription factors, BHLHB2 and BHLHB3; their gene expressions are regulated by multiple extracellular stimuli. Front. Biosci. *10*, 3151–3171.

Yan, W.X., Mirzazadeh, R., Garnerone, S., Scott, D., Schneider, M.W., Kallas, T., Custodio, J., Wernersson, E., Li, Y., Gao, L., et al. (2017). BLISS is a versatile and quantitative method for genome-wide profiling of DNA double-strand breaks. Nat. Commun. *8*, 15058.

Yu, Y., Schleich, K., Yue, B., Ji, S., Lohneis, P., Kemper, K., Silvis, M.R., Qutob, N., van Rooijen, E., Werner-Klein, M., et al. (2018). Targeting the senescence-overriding cooperative activity of structurally unrelated H3K9 demethylases in melanoma. Cancer Cell *33*, 785.

Zhang, Y., Liu, T., Meyer, C.A., Eeckhoute, J., Johnson, D.S., Bernstein, B.E., Nusbaum, C., Myers, R.M., Brown, M., Li, W., and Liu, X.S. (2008). Model-based analysis of ChIP-Seq (MACS). Genome Biol. *9*, R137.

Zhu, Y., Tchkonia, T., Pirtskhalava, T., Gower, A.C., Ding, H., Giorgadze, N., Palmer, A.K., Ikeno, Y., Hubbard, G.B., Lenburg, M., et al. (2015). The Achilles' heel of senescent cells: from transcriptome to senolytic drugs. Aging Cell *14*, 644–658.

Zhu, G., Pan, C., Bei, J.X., Li, B., Liang, C., Xu, Y., and Fu, X. (2020). Mutant p53 in Cancer Progression and Targeted Therapies. Front. Oncol. *10*, 595187.

Zirkel, A., Nikolic, M., Sofiadis, K., Mallm, G-P., Brackley, C.A., Gothe, H., Drechsel, O., Becker, C., Altmuller, J., and Josipovic, N. (2018). HMGB2 Loss upon Senescence Entry Disrupts Genomic Organization and Induces CTCF Clustering across Cell Types. Mol Cell *70*, 730–744.

STAR★METHODS

KEY RESOURCES TABLE

REAGENT or RESOURCE	SOURCE	IDENTIFIER
Antibodies		
Mouse anti-CDC6	Santa Cruz	Cat# sc-9964, RRID:AB_627236
Mouse anti-BHLHE40	Santa Cruz	Cat# sc-101023, RRID:AB_2065356
Mouse anti-BRCA1	Santa Cruz	Cat# sc-6954, RRID:AB_626761
Mouse anti-BRCA2	Sigma (mfr. Calbiochem)	Cat# OP95, RRID:AB_2067762
Mouse anti-Vinculin	Sigma	Cat# V9131, RRID:AB_477629
Rabbit anti-RAD51	Merck-Millipore	Cat# PC130, RRID:AB_2238184
Mouse anti-RAD52	Santa Cruz	Cat# sc-365341, RRID:AB_10851346
Sheep anti-RAD52	MRC-PPU Reagents, University of Dundee, Scotland	Supplied by Dr. Claudia and Jiri Lukas
Rabbit anti-RPA70	Abcam	Cat# ab79398, RRID:AB_1603759
Mouse anti-γH2AX (pSer139/140)	Abcam	Cat# ab22551, RRID:AB_447150
Mouse anti-p53	Santa Cruz	Cat# 18-7251, RRID:AB_86845
Mouse anti-MDM2	Santa Cruz	Cat# sc-965, RRID:AB_627920
Rabbit anti-PER1	Abcam	Cat#ab136451
Rabbit anti-β-actin	Cell Signaling Technology	Cat# 4967, RRID:AB_330288
Rabbit anti-GAPDH	Cell Signaling Technology	Cat# 2118, RRID:AB_561053
Rabbit-anti-HA-tag	Cell Signaling Technology	Cat# 5017, RRID:AB_10693385
Rabbit anti-53BP1	Abcam	Cat# ab36823, RRID:AB_722497
Rabbit anti-CDH1	Cell Signaling Technology	Cat# 3195, RRID:AB_2291471
Mouse anti-Vimentin	Sigma	Cat# V6630, RRID:AB_477627
Rabbit anti-H3K27ac	Active Motif	Cat# 39133, RRID:AB_2561016
Rabbit anti-H3K27me3	Active Motif	Cat# 39155, RRID:AB_2561020
Rabbit anti-Ki-67	Abcam	Cat# ab16667, RRID:AB_302459
Rabbit anti-caspase 3	Cell Signaling	Cat# 9662, RRID:AB_331439
Rabbit anti-CTCF	Active Motif	Cat# 61311, RRID:AB_2614975
Horse Radish Peroxidase-conjugated anti-mouse	Cell Signaling Technology	Cat# 7076, RRID:AB_330924
Horse Radish Peroxidase-conjugated anti-rabbit	Cell Signaling Technology	Cat# 7074, RRID:AB_2099233
Alexa Fluor 488 donkey anti-rabbit	Abcam	Cat# ab150073, RRID:AB_2636877
Alexa Fluor 568 goat anti-mouse	Abcam	Cat#ab175473
Alexa Fluor 488 goat anti-mouse	Thermo Scientific Fischer	Cat# A-11029, RRID:AB_2534088
Alexa Fluor 568 goat anti-mouse	Thermo Scientific Fischer	Cat# A-11031, RRID:AB_144696
Alexa Fluor 488 goat anti-rabbit	Thermo Scientific Fischer	Cat# A-11034, RRID:AB_2576217
Alexa Fluor 568 goat anti-rabbit	Thermo Scientific Fischer	Cat# A-11036, RRID:AB_10563566
Alexa Fluor 568 donkey anti-sheep	Thermo Scientific Fischer	Cat# A-21099, RRID:AB_2535753
Rat anti-BrdU/CldU	Bio-rad (former AbD Serotec)	Cat# OBT0030, RRID:AB_609568
Mouse anti-IdU/BrdU	Becton Dickinson	Cat# 347580, RRID:AB_10015219
Chemicals, peptides, and recombinant proteins		
Keratinocyte-Serum Free medium	Invitrogen	17005-075
Bovine pituitary extract + human epidermal growth factor (hEGF)	Invitrogen	37000-015
Doxycycline	Sigma	D9891-5G

(*Continued on next page*)

Continued

REAGENT or RESOURCE	SOURCE	IDENTIFIER
BamHI	NEB	R0136S
SmaI	NEB	R0141S
BbSI	NEB	R0539S
5,6-dichloro-1-β-D-ribofuranosylbenzimidazole (DRB)	Merck	287891
Laemmli buffer	Merck	38733
polyvinylidene fluoride (PVDF) membrane	Macherey-Nagel	741260
Clarity Western ECL Substrate	Bio-rad	1705060
SenTraGor ™	Supplied by Lab Supplies Scientific	N/A
5-ethynyl-2′-deoxyuridine (EdU)	Invitrogen	A10044
diamidino-2-phenylindole (DAPI)	Thermo Fisher Scientific	62248
5-Iodo-2′-deoxyuridine (IdU)	Sigma-Aldrich	I7125
5-Chloro-2′-deoxyuridine (CldU)	Sigma-Aldrich	C6891
5-bromo-2′-deoxyuridine (BrdU)	Sigma-Aldrich	B5002
Effectene Transfection Reagent	QIAGEN	301425
Trizol	Thermo Fisher Scientific	15596026
Phosphate Buffer Saline (PBS) 1X	Biowest	L0615-500
Triton X-100	Acros Organics	327372500
FuGENE ® HD Transfection Reagent	Promega	E2311
Trypsin/ Ethylenediaminetetraacetic acid (EDTA) 10x	Thermo Fisher Scientific	15400054
Trypsin Neutralizer Solution	Thermo Fisher Scientific	R002100
Fetal Bovine Serum (FBS)	GIBCO	10270-106
Bovine Serum Albumin (BSA)	Applichem	A1391
Proteinase K	Thermo Fisher Scientific	AM2548
Paraformaldehyde (PFA)	Merck	104005
Glycine	Applichem	A1067
Lipofectamine RNAiMAX Transfection Reagent	Thermo Fisher Scientific	13778150
Critical commercial assays		
Click-iT Alexa Fluor 647 Imaging Kit	Thermo Fisher Scientific	C10340
Direct-zol RNA miniprep kit	Zymo Research	R2050
TruSeq RNA library kit	Illumina	RS-122-2001
Arima Hi-C kit	Arima Genomics	A51008-ARI
QIAquick PCR Purification Kit	QIAGEN	28104
Deposited data		
All Hi-C data have been uploaded on NCBI Gene Expression Omnibus repository	This paper	GSE163371
All other data have been uploaded on Sequence Read Archive	This paper	bioproject PRJNA685322
Raw data from Figures 1, 2, 3, 5, 6, S1, and S4–S6 were deposited on Mendeley	This paper	https://doi.org/10.17632/9dhvmhy98s.1
Experimental models: Cell lines		
HBEC-CDC6 Tet-ON	Ramirez et al., 2003; Komseli et al., 2018	Supplied by Liloglou T. (parental cells known as HBEC-3KT Constructed by our group
HPDEC-CDC6 Tet-ON	Furukawa et al., 1996	Supplied by Townsend P.

(*Continued on next page*)

Continued

REAGENT or RESOURCE	SOURCE	IDENTIFIER
Oligonucleotides		
Primers for the screening of inverted clones, see Table S4	This paper	N/A
Primers and full Sanger sequences, see Table S4	This paper	N/A
gRNA1, see Table S4	This paper	N/A
gRNA2, see Table S4	This paper	N/A
siRNA cocktail targeting BHLHE40	Origene	Cat No SR305619
siRNA cocktail targeting BHLHE40	Thermo Fisher Scientific	Cat No 1299001: HSS112516, HSS112517, HSS112518
Recombinant DNA		
pcDNA3-HA-BHLHE40	Addgene	RRID:Addgene_110154
pcDNA3 Hygro HA Akt2	Addgene	RRID:Addgene_16000
DR-GFP	Stark et al., 2004	Supplied by Halazonetis T.
BIR-GFP	Sotiriou et al., 2016	Supplied by Halazonetis T.
SA-GFP	Stark et al., 2004	Supplied by Halazonetis T.
HA-ISceID44A	Galanos et al., 2018	Supplied by Soutoglou E.
pSpCas9(BB)-2A-GFP (PX458)	Addgene	RRID:Addgene_48138
pU6-(BbsI)_CBh-Cas9-T2A-mCherry	Addgene	RRID:Addgene_64324
Software and algorithms		
ScanR automated image acquisition and analysis software (Olympus, 3.1)	Olympus	https://www.olympus-lifescience.com/en/microscopes/inverted/scanr/
TIBCO Spotfire Analyst, version 10.10.3	Tibco Software	https://perkinelmerinformatics.com/products/exclusive-reseller/tibco-spotfire/
STAR aligner (version 2.5.3a)	Dobin et al., 2013	https://github.com/alexdobin/STAR
Samtools (version 0.1.19)	Li et al., 2009	http://samtools.sourceforge.net/
HTseq count (version 0.5.4p3.)	Anders et al., 2015	https://htseq.readthedocs.io/en/master/history.html
RUVseq	Risso et al., 2014	https://rdrr.io/bioc/RUVSeq/man/RUVr.html
DESeq	Anders and Huber, 2010	https://www.bioconductor.org/packages//2.10/bioc/html/DESeq.html
BWA-MEM	Li and Durbin, 2010	http://bio-bwa.sourceforge.net/
MACS2 (ver. 2.1.2)	Zhang et al., 2008	https://pypi.org/project/MACS2/
Bowtie (ver. 23.4.1)	Langmead and Salzberg, 2012	https://sourceforge.net/projects/bowtie-bio/files/bowtie2/2.3.4.1/
HiCExplorer (ver. 3.2)	Ramírez et al., 2018	https://github.com/deeptools/HiCExplorer
Knight-Ruiz (KR) matrix balancing algorithm	Knight and Ruiz, 2013	https://github.com/deeptools/Knight-Ruiz-Matrix-balancing-algorithm
HiGlass	Kerpedjiev et al., 2018	https://higlass.io/
Cooler	Abdennur and Mirny, 2020	https://github.com/open2c/cooler
MANTA	Chen et al., 2016	https://github.com/Illumina/manta
ANNOVAR	Wang et al., 2010	https://annovar.openbioinformatics.org/en/latest/
Bcftools	Li et al., 2009	https://github.com/samtools/bcftools
GATK tools	Van der Auwera et al., 2013	https://gatk.broadinstitute.org/hc/en-us
Other		
Matrigel Invasion Chambers	Corning	354480
Neubauer glass chamber	Marienfeld Superior	0640010
Kodak® BioMax® MS film	Merck	Z363030-50EA

RESOURCE AVAILABILITY

Lead contact

Further information and requests for resources and reagents should be directed to and will be fulfilled by the Lead Contact, Vassilis Gorgoulis (vgorg@med.uoa.gr)

Materials availability

This study did not generate any unique reagents.

Data and code availability

- All Hi-C data generated in this study have been deposited at GEO and are publicly available as of the date of publication. Accession numbers are listed in the Key resources table. Original western blot images have been deposited at Mendeley and are publicly available as of the date of publication. The DOI is listed in the Key resources table. Microscopy data reported in this paper will be shared by the lead contact upon request.
- This paper does not report original code.
- Any additional information required to reanalyze the data reported in this paper is available from the lead contact upon request.

All the Hi-C data generated in this study are available via the NCBI Gene Expression Omnibus repository under accession number GSE163371 (reviewer access token: *kfmxuuaxnklzqd*). All the other data are available via the Sequence Read Archive under bioproject PRJNA685322.

Raw data from Figures 1, 2, 3, 5, 6, S1, and S4–S6 were deposited on Mendeley at [https://doi.org/10.17632/9dhvmhy98s.1].

EXPERIMENTAL MODEL AND SUBJECT DETAILS

Human female HBEC-CDC6 Tet-ON and HPDEC-CDC6 Tet-ON cell lines were maintained in Keratinocyte-Serum-Free Medium (17005-075, Invitrogen) supplemented with 50 μg/ml Bovine Pituitary Extract and 5ng/ml hEGF (37000-015, Invitrogen) at 37°C and 5% CO_2 (Komseli et al., 2018). *CDC6* induction was conducted by treatment of the cell culture with 1 μg/ml doxycycline hyclate (DOX) (Sigma). Where applied, 5,6-dichloro-1-β-D-ribofuranosylbenzimidazole (DRB, Merck) was used at a final concentration of 100μM and it was added directly in the growth media for the indicated time periods. The cell lines used in this study were not found in the database of commonly misidentified cell lines that is maintained by ICLAC and NCBI Biosample. Its identity has been authenticated by STR profiling and is regularly tested for mycoplasma.

METHOD DETAILS

Plasmid generation

The pcDNA3-HA-BHLHE40 vector was obtained from Addgene (cat No 110154). The neomycin resistance cassette was replaced with a hygromycin coding one. The hygro insert was amplified through fusion-PCR from a pcDNA3 Hygro HA Akt2 vector (Addgene Cat No 16000). Moreover, a pcDNA3 Hygro vector with no insert was generated for mock experiments.

siRNA and plasmid transfections

For BHLHE40 silencing two different cocktails of 3 unique siRNA duplexes - 2 nmol each from OriGene Technologies, Inc, (Cat No SR305619) and from Thermo Fisher Scientific (#1299001: HSS112516, HSS112517, HSS112518) were employed respectively, to secure off-target effects. siRNA gene silencing was performed as previously described, following also the manufacturer's instructions (Galanos et al., 2016). More specifically, 3×10^5 cells plated in 60mm dishes were transfected using Invitrogen Lipofectamine RNAiMAX Transfection Reagent (#13778150) with the appropriate RNAi pool (set of three siRNAs) or the corresponding RNAi negative control. Cells were harvested 48h after transfection for further analysis.

Selection of escaped clones

Initially, $5x10^5$ cells were plated. One day after the plating, CDC6 expression is induced by adding doxycycline in the culture media. Following the induction, cells fully senesce at day 6. At about day 30, senescence-evading cells start forming roughly 50 distinct colonies. Eventually, colonies were collected and they were transferred to 6-well plates, where they independently propagated.

Protein extraction, cell fractionation and immunoblot analysis

Total protein extracts were obtained by resuspension in 50 mM Tris/HCl pH 8.0, 150 mM NaCl, 0,1% SDS, 0,5% sodium deoxycholate, 1% NP-40 adjusted with protease and phosphatase inhibitors and rotation for 1 h at 4°C. The lysate was centrifuged at 13,400 rpm at 4°C for 15 min. The supernatant was collected and proteins quantified using Protein assay dye concentrate (BIO-RAD). Thirty micrograms of protein from total extracts per sample were adjusted with Laemmli buffer (Merck, 38733) and loaded on acrylamide/bis-acrylamide gels. Gel electrophoresis was followed by transfer to PVDF membrane (Macherey-Nagel, 741260), while signal

development was carried out by Clarity Western ECL Substrate (Bio-rad, 1705060) chemiluminescence and captured by using either autoradiography films (Kodak® BioMax® MS film) or on an iBright CL750 Imaging System (Thermo Fisher Scientific). Horse Radish Peroxidase conjugated anti-mouse and anti-rabbit secondary antibodies (1:1000 dilution) (Cell Signaling) were used.

Primary antibodies utilized were: anti-CDC6 (mouse, Santa Cruz, sc9964, 1:500), anti-BHLHE40 (mouse, Santa Cruz, sc101023, 1:200), anti-RAD52 (mouse, Santa Cruz, sc-365341, 1:100), anti-RAD51 (rabbit, Merck-Millipore, PC130, 1:100), anti-BRCA1 (mouse, Santa Cruz, sc6954, 1:500), anti-BRCA2 (mouse, Sigma (mfr. Calbiochem), OP95, 1:500), anti-p53 (mouse, Santa Cruz, DO7, 1:500), anti-MDM2 (mouse, Santa Cruz, SMP14, 1:500), anti-PER1 (rabbit, Abcam, ab136451, 1:500), anti-β-actin (rabbit, Cell Signaling, 4967L, 1:1000), anti-GAPDH (rabbit, Cell Signaling, 2118S, 1:2000), anti-vinculin (mouse, Sigma, V9131, 1:1000), anti-HA-Tag (C29F4 rabbit, Cell Signaling, 3724, 1:1000). All analyses were performed in triplicate.

Immunofluorescence analysis

Indirect immunofluorescence analysis was performed as previously described (Galanos et al., 2018). Specifically, cells were seeded and grown on 12-mm diameter autoclaved glass coverslips. To identify RAD52, RPA70, 53BP1 and γH2AX foci, cells were pre-extracted on ice with cold PBS containing 0.1% Triton X-100 for 5 min before fixation in 4% cold formaldehyde solution for 15 min at room temperature. For the rest of the analyzed proteins, the pre-extraction step was skipped. When Click-iT EdU staining was performed, cells were incubated with 10 μM EdU for 30 min, before fixation or pre-extraction. Detection of EdU was performed according to the manufacturer's recommendations (Click-iT Imaging Kit Alexa Fluor 647; Thermo Fisher Scientific, C10340) followed by incubation with primary antibodies. Cells were incubated with primary antibodies for 1 h at room temperature. Following washing steps with PBS, coverslips were incubated with the corresponding secondary antibodies (Thermo Fischer Scientific) supplemented with DAPI for an additional 1 h at room temperature before washed again and mounted. Image acquisition of multiple random fields was automated on a DM 6000 CFS Upright Microscope (Confocal Leica TCS SP5 II) or a ScanR screening station (Olympus) and analyzed with ScanR (Olympus) software, or a Zeiss Axiolab fluorescence microscope equipped with a Zeiss Axiocam MRm camera and Achroplan objectives, while image acquisition was performed with AxioVision software 4.7.1. In the case of RAD52, the representative images of foci formation (presented in Figure 3Ci) were acquired with a confocal LSM800 Zeiss microscope and processed with its Blue ZEN software. Primary antibodies utilized were: anti-CDC6 (mouse, Santa Cruz, sc9964, 1:500), anti-RAD52 (sheep, MRC-PPU Reagents, 1:100, kind gift from Drs. Jiri and Claudia Lukas), anti-53BP1 (rabbit polyclonal, Abcam ab36823, 1:250), anti-CDH1 (E-cadherin) (rabbit monoclonal, Cell Signaling #3195S, 1:100), anti-Vimentin (mouse monoclonal, Sigma V6630, 1:100), anti-RPA70 (rabbit, Abcam, ab79398, 1:100), anti-γH2AX (mouse monoclonal, Abcam, ab22551, 1:100). All analyses were performed in triplicate.

Immunocytochemistry

For immunocytochemistry analysis cells were grown on coverslips and fixed with 100% ice-cold methanol or 4% formaldehyde (prepared from paraformaldehyde) for 10 min and stored at 4°C until staining was performed. Following, cells were permeabilized with 0,3% Triton X-100 in PBS for 5 min at RT. A 10% fetal bovine serum and 3% bovine serum albumin in PBS solution was used as a blocking buffer for 1 h at RT. Primary antibodies were diluted in blocking buffer and incubated overnight at 4°C. Secondary antibodies were: Ki-67 (rabbit, Abcam, ab16667, 1:250), caspase 3 (rabbit, Cell Signaling, 9662, 1:500). Nuclear signal was evaluated as a positive one. A minimum of 100 cells were counted at high power optical field (x 400).

Cell growth analysis

HBEC cells were seeded at day 0 on 6-well plates at a density of 8×10^4 cells per well. Every day up to day 6, cells from one well at a time were trypsinized and counted using a standard Neubauer chamber (Marienfeld Superior, # 0640010).

3D (organotypic) culture

First, airway fibroblasts were embedded in type I collagen, allowing contraction of the gel mimicking the underlying submucosa, as previously described (Sato et al., 2006; Ramirez et al., 2003; Lagopati et al., 2021). Briefly, positively selected HBEC-CDC6 Tet-ON cells were seeded on top of the contracted layer and upon attachment of HBECs on the underlying stroma, the organotypic culture was submerged into Keratinocyte-Serum-Free Medium (#17005-075, Invitrogen) supplemented with 50 μg/ml Bovine Pituitary Extract and 5ng/ml hEGF (#17005-075, Invitrogen) and then lifted to an air-liquid interface, while cell growth was performed at 37°C with 5% CO_2. Following, *CDC6* induction was performed as per the 2D culture medium. Finally, matrigels were collected at 6 and 30 days post-induction, formalin fixed and paraffin embedded. Sections were obtained and processed for hematoxylin-eosin and GL13 staining and immunohistochemical analysis as described in previous section.

Senescence detection with SenTraGor

Sentragor™ staining was performed and evaluated according to previous published protocols (Evangelou et al., 2017, Gorgoulis et al., 2019; Kohli et al., 2021). Specifically, fixed cells mounted on coverslips were rinsed sequentially in 50% and 70% Ethanol for 5 minutes at room temperature, respectively. Then the coverslips were incubated with the SenTraGor™ solution for 10 minutes. Following washings with 50% Ethanol and TBS at room temperature, the anti-biotin antibody ([Hyb-8] ab201341 Abcam, diluted 1:30 in TBS) was applied for 60 minutes at 37°C. Subsequently the signal was developed using the Ultravision Quanto Detection System

HRP DAB kit (Cat no: TL-125-QHD), according to the manufacturer's instructions. Finally cells were counterstained with Hematoxylin (diluted 1:4 in deionized water) for 40 s and observed under a light microscope.

Invasion assay

Invasion assay was performed as described elsewhere (Sideridou et al., 2011; Galanos et al., 2016). Cells were trypsinized and plated ($1x10^5$) into a cell invasionchamber (Corning, 354480) containing EGF-free medium and allowed to invade for 24h toward full medium. Cells were fixed with 4% paraformaldehyde, stained with Giemsa, photographed and counted. Data from three independent measurements were averaged, and the corresponding SDs are also reported.

Tumorigenicity assay

Tumorigenicity assay was performed as previously described (Liontos et al., 2007). In brief, ESC and OFF cells were collected, washed in PBS, and s.c. injected (2×10^6 cells) at two opposite sites in the abdominal region of the same male severe combined immunodeficient (SCID) mouse, respectively. Two animals were tested. Tumor growth was measured twice to thrice weekly.

Flow cytometry analysis (FACS) - Cell Cycle analysis

Cell cycle analysis was determined using a BD FACSVerse (BD Biosciences), following EdU incorporation, as previously published (Galanos et al., 2016). Briefly, cells were incubated with 10 μM EdU for 30 min, and they were then fixed with 70% of ice cold ethanol and were incubated on ice for at least 30 min or kept at −20°C until the day of staining and analysis. Afterward, the samples were centrifuged (1500 rpm, 5 min at room temperature) and washed sequentially with PBS and PBS^+ (PBS, 1% BSA and 0,1% Tween). Detection of EdU was performed according to the manufacturer's recommendations (Click-iT Imaging Kit Alexa Fluor 647; Thermo Fisher Scientific, C10340) and subsequently samples were incubated with Hoechst 33342 (1:1000 in PBS) followed by a final wash with PBS^+. Cells were then analyzed on BD FACSVerse (BD Biosciences) and acquired data were processed using the FlowJo software.

5′-EU incorporation based nascent RNA assay

In situ detection of nascent RNA was performed with the Click-iT Alexa Fluor 488 Imaging Kit (Thermo Fisher Scientific) as described elsewhere (Komseli et al., 2018).

QIBC analysis

Quantitative image-based cytometry (QIBC) analysis (Figure S2) was performed essentially as previously described (Ochs et al., 2016). In brief, images were taken with a ScanR inverted microscope High-content Screening Station (Olympus) for Life Science that was equipped with wide-field optics, 20x or 40x dry objectives were used, fast excitation and emission filter-wheel devices for 6 different spectral wavelength areas, an MT20 illumination system, and a digital monochrome scientific CMOS camera with sensor chip FL-400. Images were obtained in an automated fashion with the ScanR acquisition software (Olympus, 3.2.0). For each condition, 81 to 100 images were acquired containing at least 2,000 cells per condition. Acquisition times for the different channels were adjusted for non-saturated conditions, and same settings were applied to all the samples within one experiment. Images were processed and analyzed with the corresponding ScanR analysis software. In brief, the DAPI signal was used for the generation of an intensity-threshold-based mask to identify individual nuclei as main objects. This mask was then applied to analyze pixel intensities in different channels for each individual nucleus. For analysis of DNA damage-induced foci, additional masks were generated by segmentation of the respective images into individual spots with intensity-based or spot-detector modules provide by the software. Foci were defined as sub-objects, and the generated mask was used for quantification of pixel mean intensities in foci. Based on the distinguished objects and sub-objects, the desired parameters (mean and total intensities, area, foci count, and foci intensities) for the each nuclei or foci were quantified, as well as derived parameters (sum of foci intensity per nucleus). These values were then exported as .txt files and analyzed with TIBCO Software (version 10.10.0). This software was used to quantify absolute, median, and average values in cell populations and to generate all color-coded scatterplots. Within one experiment, similar cell numbers were compared for the different conditions. Primary antibodies utilized were: anti-53BP1 (rabbit, Abcam ab36823, 1:250), anti-γH2AX (pSer139/140) (rabbit, Abcam, ab36823, 1:100), anti-RPA (rabbit, Abcam, ab79398, 1:100), anti-RAD52 (sheep, MRC-PPU Reagents, 1:100, kind gift from Drs. Jiri and Claudia Lukas).

DR-GFP, SA-GFP and BIR-GFP reporter assays

HBEC-CDC6 Tet-ON cells were transiently transfected with the GFP based reporter constructs for synthesis-dependent strand annealing (DR-GFP), single strand annealing (SA-GFP) and break induced replication (BIR-GFP), as previously described (Galanos et al., 2018). To monitor repair of I-*Sce*I- generated DSBs, cells were transiently co-transfected with 1 μg of the I-*Sce*I expression vector HA-ISceID44A (Addgene #59424) using the Effectene reagent (QIAGEN). DSB repair efficiency upon *CDC6* induction was determined by quantifying GFP-positive cells via flow cytometry FACS Calibur (Becton Dickinson) 48h after transfection, under non-chromatinized conditions.

DNA fiber fluorography (combing assay)

The assay was conducted as previously described (Galanos et al., 2016). Briefly, HBEC-CDC6 Tet-ON cells were grown in the presence or absence of doxycycline for the indicated time points (see Figure 2B) and then pulsed-labeled with 25 μM CldU for 20min, and

then labeled with 250 μM IdU for 20min (1:1000, I7125, Sigma-Aldrich). Cells were then harvested and lysed on glass slides in spreading buffer, DNA was denatured and stained using rat anti-BrdU/CldU (1:1000, C6891, B5002, Sigma-Aldrich) and mouse anti-IdU/BrdU (1:500, clone B44, Becton Dickinson) antibodies.

Breaks Labeling *In Situ* and Sequencing (BLISS)

''Breaks Labeling In Situ and Sequencing'' (BLISS) analysis was performed as previously described (Yan et al., 2017; Bouwman et al., 2020). Briefly, the method consists of following main steps: i) upon harvesting of cells from multi-well plates, approx. 2 million cells were fixed in suspension with 4% formaldehyde for 10 min at room temperature, ii) DSBs ends were *in situ* blunted, iii) next they were tagged with dsDNA adapters containing sample barcodes, UMIS (unique molecular identifiers), RA5 adaptor and T7 promoter, iv) tagged DSB ends were linearly amplified using *in vitro* transcription and v) the resulting RNA was used for library preparation and sequencing. BLISS data were analyzed as described below.

Next Generation Sequencing and Bioinformatics analysis

For whole-genome sequencing (WGS), library preparations were as described previously (Galanos et al., 2018). SAMtools *mpileup* and *bcftools* (Li et al., 2009), *GATK tools*, the GATK source bundle and the GATK best practices guide (Van der Auwera et al., 2013), were used for identification and filtering of the SNPs and INDELs. Variations that were unique in the ''escaped'' cells were normalized based on the sequencing depth of each experiment. Copy number and structural variants were determined using MANTA (Chen et al., 2016) and annotated on the Human reference genome using ANNOVAR (Wang et al., 2010). As shared CNVs (or overlapped regions) we characterized the common intersected variations between the escape replicates, (using intersectBed -wa -u from BEDtools), after extracting the variations that are present in the OFF samples (intersectBed -v). A detailed description, on the intersected CNVs, among the precise coordinates of all CNVs is reported in the new Table S1. The depth of coverage that was obtained for each sample is described in Table S4B.

For BLISS data, DNA Double Stranded Breaks (DSBs) were normalized for total mapped reads and for the total number of used cells for each replicate. The aggregation of Unique Molecule Identifiers (UMIs) and the frequency of DSBs in various genomic regions were calculated using in-house R scripts (available on request).

BLISS signal data and CNV regions were compared with intersectBed, a subcommand from BEDtools suite in order to determine the distribution of expected overlaps. As a control we used a randomly selected set of loci by applying the randomBed and shuffleBed subcommands in order to permute these genomic locations repeatedly (10000 times).

RNA isolation, sequencing, and data analysis

6-day ON and senescence-bypass ''inverted'' HBECs were harvested in Trizol (Thermo Fisher Scientific, 15596026) and total RNA was isolated and DNase-treated using the Direct-zol RNA miniprep kit (Zymo Research) as per manufacturer's instructions. cDNA libraries were next generated using the TruSeq RNA library kit (Illumina) via selection on poly(dT) beads. The resulting libraries were single-end sequenced to > 50 million reads on a HiSeq4000 platform (Illumina). Raw reads were mapped to the human genome (hg19) using STAR aligner (version 2.5.3a) (Dobin et al., 2013). Samtools (version 0.1.19) (Li et al., 2009) were used for data filtering and file format conversion, while HTseq count (version 0.5.4p3.) algorithm (Anders et al., 2015) was used to assign aligned reads to exons using the following command line «htseq-count –s no –m intersection -nonempty». Normalization of reads and removal of unwanted variation was performed with RUVseq (Risso et al., 2014). Differential gene expression was computed using DESeq (Anders and Huber, 2010), and significantly deregulated genes (fold change cut-off 1.5 and P value $\leq$ 0.05) are listed in Table S5.

Chromatin immunoprecipitation (ChIP), sequencing, and data analysis

ChIP was performed on 10-15 million cells crosslinked in 1% PFA/PBS at RT for 10 min, and quenched in 0.125M ice-cold glycine. ChIP material was prepared as previously described (Ford et al., 2014), and sonication was performed using a Bioruptor sonicator and adjusting fragment size to 200-500 bp. For the IP the following polyclonal antisera were used: anti-CTCF (61311, Active Motif), anti-H3K27ac (39133, Active Motif), anti-H3K27me3 (39155, Active Motif) and anti-BHLHE40 (#NB100-800, Novus Biologicals). ChIP-seq libraries were sequenced on a HiSeq4000 platform (Illumina) to at least 25 million reads per sample, and analyzed using the ENCODE pipeline (https://www.encodeproject.org/chip-seq/transcription_factor/).

Genome-wide chromosome conformation capture (Hi-C) and data analysis

In situ Hi-C on HBECs of different states and genotypes was performed and controlled for quality using the Arima Hi-C kit as per manufacturer's instructions. All resulting libraries that met the QC criteria set by the manufacturer were paired-end sequenced on a NovoSeq6000 platform (Illumina) to at least 0.5 billion reads. For data analysis, reads were mapped to the reference human genome (GRCh37/hg19) using Bowtie (ver. 23.4.1) (Langmead and Salzberg, 2012) with the ''–reorder'' flag. Local mapping was used to increase mapping rates due to the inherent presence of chimeric reads. All preprocessing and downstream analysis was performed using HiCExplorer (ver. 3.2) (Ramírez et al., 2018) to remove unmappable reads, non-uniquely mapped reads and low-mapping-quality reads, as well as duplicated pairs (i.e., starting and ending with exactly the same location), dangling-ends (i.e., digested but not ligated), self-circularized (i.e., reads pairing within < 25 Kbp and facing outward), same-fragment (i.e., read pair locating in the same restriction enzyme fragment) or self-ligated reads (i.e., having a restriction site in between the read pair within < 800 bp). Next,

genome-wide contact matrices were generated in the form of *.cool* files, in which the genome was binned into different sizes (resolution) — 10 kb, 20 kb, 50 kb and 100 kb — for different downstream usage. To facilitate comparison between different samples, all Hi-C interaction counts were normalized and then balanced using the Knight-Ruiz (KR) matrix balancing algorithm (Knight and Ruiz 2013). Hi-C matrices stored in *.cool* files were visualized using HiGlass (Kerpedjiev et al., 2018) as interactive heatmaps. To make zooming-in and -out possible, normalized and balanced *.cool* files at 10 Kbp resolution were converted to multi-resolution cooler files called *.mcool* files using Cooler (Abdennur and Mirny 2020). For calling A/B compartments, 100 kbp-resolution and Pearson-transformed matrices were used to calculate the first eigenvector, which was then integrated with own H3K27ac ChIP-seq data to mark A-compartments. TADs were assigned using 20 kbp-resolution matrices using the function embedded in HiCExplorer based on deduced *z*-scores and with a *P*-value cutoff of 0.01. Finally, loops we detected as previously described (Rao et al., 2014) by computing a negative binomial distribution of 10 kbp-resolution Hi-C data and using Anderson-Darling/Wilcoxon rank-sum tests and a *P*-value cutoff of 0.05; loop lengths were restricted to 0.1-2 Mbp (to avoid signal contamination from the diagonal of Hi-C matrices), and compared to CTCF ChIP-seq data to identify loops with CTCF-bound anchors.

CRISPR/Cas9 inversion generation

Design of gRNAs

Based on the WGS data (see corresponding section), 20-nt sgRNAs were designed around each breakpoint. Two complementary DNA oligos for each sgRNA were annealed generating 5′overhangs consisting of CACC(G) and AAAC. gRNA1 and gRNA2 were chosen due to high specificity and small distance from the exact breakpoints (Table S4). They were cloned into – Cas9 expression plasmids - pSpCas9(BB)-2A-GFP (PX458) and pU6-(BbsI)_CBh-Cas9-T2A-mCherry, respectively, which had been already digested with BbsI. In this way, sgRNAs were integrated next to the gRNA scaffold of the particular vector (Figure S6A) (Table S4).

Transfection and FACS sorting

HBECs were cultured in Keratinocyte (serum free medium) (#17005042) without antibiotics supplemented with 25 mg Bovine Pituitary Extract and 2.5 μg EGF, Human Recombinant. Delivery of 2.5 μg from each plasmid, coding for one sgRNA and Cas9, was performed via double transfection of HBECs two days after plating $8x10^4$ cells per well in a 6-well plate (reaching 80% confluency) with FuGENE ® HD Transfection Reagent (Promega #E2311) (4:1 FuGENE® HD Transfection Reagent: DNA Ratio). FACS sorting of double positive (GFP and mCherry) cells gave rise to a large number of clones, subsequently cultured in 96-well plates (Figure S6A).

DNA extraction and PCR screening

After harvesting cells from 96-well plates in 30 μL Trypsin/EDTA 1x (stock 10X, Thermo Fisher Scientific, #15400054), followed by a neutralization step with an equal volume of Trypsin Neutralizer Solution (Thermo Fisher Scientific, #R002100), half of the cells were lysed by adding 30 μL of Lysis Buffer (50 mM KCl, 1 0mM TRIS pH: 8.3, 2.5 mM $MgCl_2$, 0.45% NP40 and 0.45% Tween20) containing Proteinase K (1 μL of 20 μg/μl Proteinase K for every 50 μL of Lysis Buffer), and heating for 45 min at 60°C followed by 10 min at 80°C to inactivate Proteinase K. The other half of the cells were kept in culture. 4 μL of the lysate were used as genomic DNA for PCR. Two pairs of forward and reverse primer were designed around each breakpoint (Table S4). PCR product of F1/R1 and F2/R2 manifest the wild-type genomic DNA, while F1/F2 and R1/R2 give product in case that the area has been inverted. PCR products were submitted for Sanger sequencing verification (Figure 6A and S6A).

Sanger sequencing

PCR products were purified using the QIAquick PCR Purification Kit (#28104) and submitted for Sanger sequencing. Parental HBEC-CDC6 Tet-ON cells were used as a reference. Primers and full Sanger sequences are available in Table S4.

Survival data analysis

Data on survival analysis was obtained from a public database Kaplan-Meier plotter (http://www.kmplot.com; Nagy et al., 2018), except for breast and prostate cancer data for which a separate Log-rank (Mantel-Cox) survival analysis, with Bonferroni correction, was performed on data retrieved from Metabric and TCGA, respectively.

QUANTIFICATION AND STATISTICAL ANALYSIS

Two-tailed unpaired Student's t test was employed to compare data obtained by DNA fiber fluorography, QiBC assay, immunofluorescence imaging, reporter assays and differences in cell proliferation and invasion assay.

Super Exact test was used to assess whether common CNVs were significantly more than expected by chance,

The hypergeometric test was applied to estimate the significance of the upregulated genes which were identified as both BHLHE40 target genes and differentially expressed genes during escape.

Fisher's exact test was used to assess the significance of the increased cell death in FACS-based cell cycle profiling and in the immunostaining for Caspase-3.

Wilcoxon-Mann-Whitney test was used to examine changes in the distribution of lengths for the loops observed.

Molecular Cell, Volume *81*

Supplemental information

A recurrent chromosomal inversion suffices for driving escape from oncogene-induced senescence via subTAD reorganization

Christos P. Zampetidis, Panagiotis Galanos, Andriani Angelopoulou, Yajie Zhu, Aikaterini Polyzou, Timokratis Karamitros, Athanassios Kotsinas, Nefeli Lagopati, Ioanna Mourkioti, Reza Mirzazadeh, Alexandros Polyzos, Silvano Garnerone, Athanasia Mizi, Eduardo G. Gusmao, Konstantinos Sofiadis, Zita Gál, Dorthe H. Larsen, Dafni-Eleftheria Pefani, Marco Demaria, Aristotelis Tsirigos, Nicola Crosetto, Apolinar Maya-Mendoza, Angelos Papaspyropoulos, Konstantinos Evangelou, Jiri Bartek, Argyris Papantonis, and Vassilis G. Gorgoulis

Supplemental Information / Supplemental figure and table legends

A recurrent chromosomal inversion suffices for driving escape from oncogene-induced senescence via subTAD reorganization

Zampetidis CP, Galanos P, Angelopoulou A, Zhu Y, Polyzou A, Karamitros T, Kotsinas A, Lagopati N, Mourkioti I, Mirzazadeh R, Polyzos A, Garnerone S, Mizi A, Gusmao EG, Sofiadis K, Gál Z, Larsen DH, Pefani DE, Demaria M, Tsirigos A, Crosetto N, Maya-Mendoza A, Papaspyropoulos A, Evangelou K, Bartek J, Papantonis A, Gorgoulis VG

SUPPLEMENTAL FIGURES

Figure S1

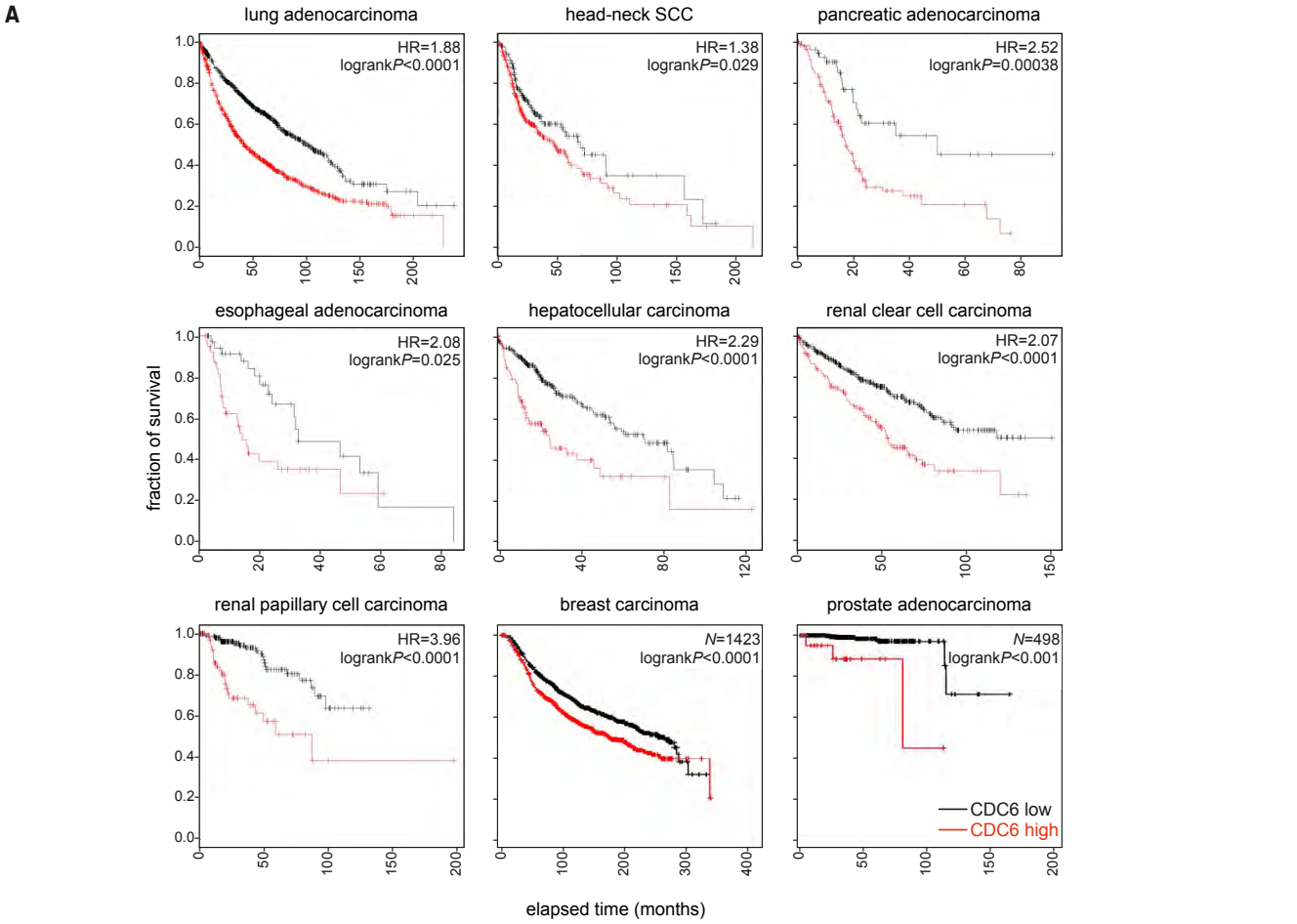
A
lung adenocarcinoma
HR=1.88
logrankP<0.0001
head-neck SCC
HR=1.38
logrankP=0.029
pancreatic adenocarcinoma
HR=2.52
logrankP=0.00038
esophageal adenocarcinoma
HR=2.08
logrankP=0.025
hepatocellular carcinoma
HR=2.29
logrankP<0.0001
renal clear cell carcinoma
HR=2.07
logrankP<0.0001
renal papillary cell carcinoma
HR=3.96
logrankP<0.0001
breast carcinoma
N=1423
logrankP<0.0001
prostate adenocarcinoma
N=498
logrankP<0.001
CDC6 low
CDC6 high
fraction of survival
elapsed time (months)

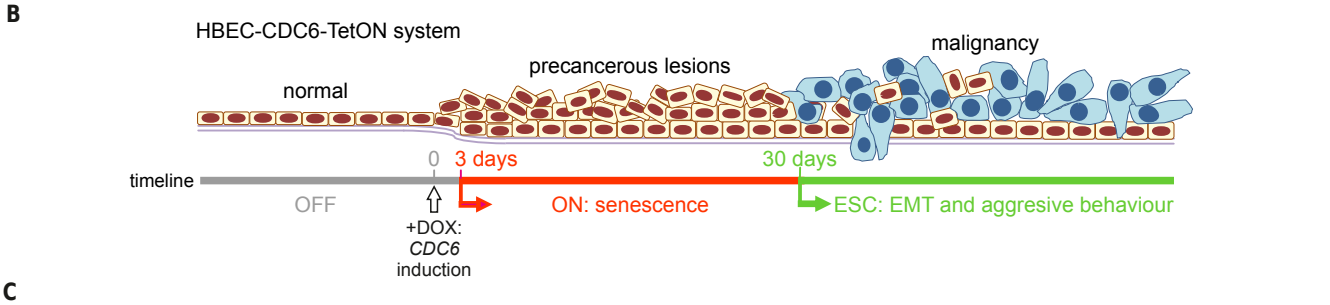
B
HBEC-CDC6-TetON system
normal
precancerous lesions
malignancy
timeline
0
3 days
30 days
OFF
+DOX:
CDC6
induction
ON: senescence
ESC: EMT and aggresive behaviour

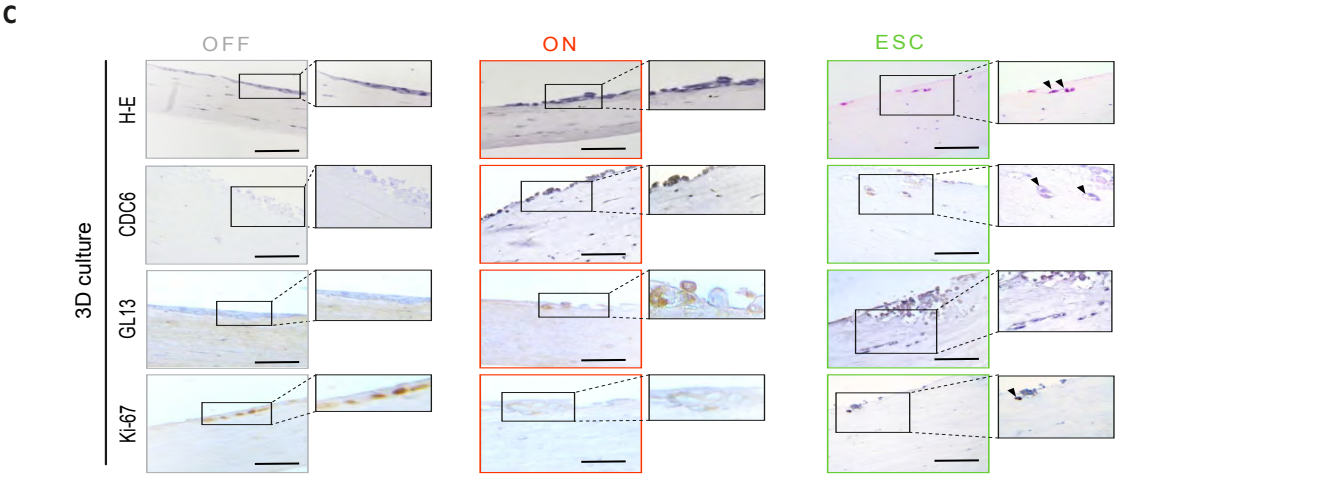
C
OFF
ON
ESC
3D culture
H-E
CDC6
GL13
Ki-67

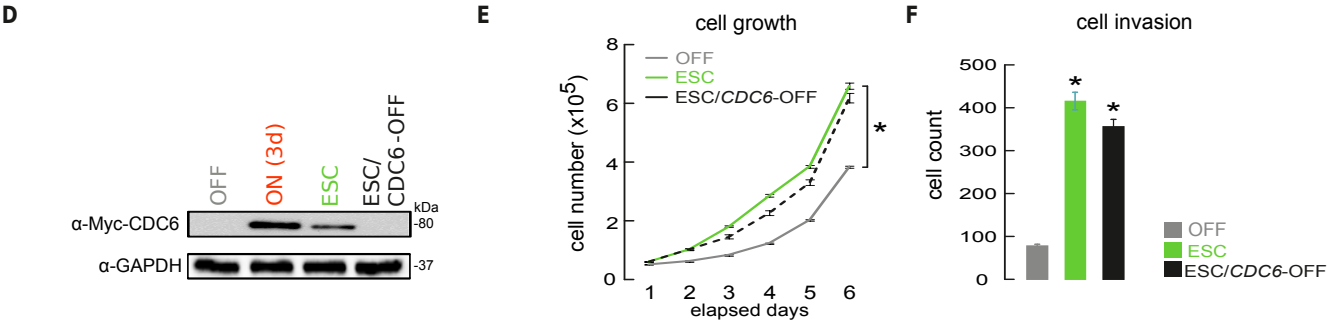
D
OFF
ON (3d)
ESC
ESC/
CDC6 -OFF
kDa
α-Myc-CDC6
-80
α-GAPDH
-37
E
cell growth
OFF
ESC
ESC/CDC6-OFF
cell number (x10^5)
elapsed days
F
cell invasion
cell count
OFF
ESC
ESC/CDC6-OFF

Figure S2

Workflow of Quantitative Image - Based Cytometry (QIBC)

Image Acquisition

Inverted Motorized Research Microscope Olympus IX83

Image Analysis

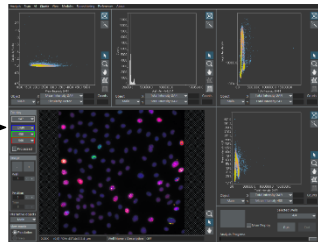

Olympus Scan® Automated Image Acquisition Software

DNA staining

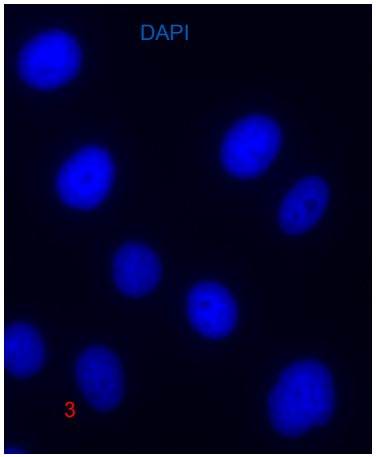

Cell Cycle profile

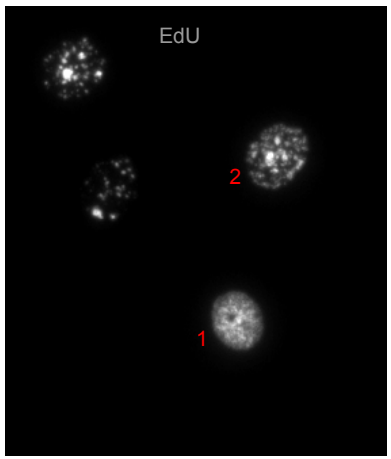

Step 1

Cell cycle distribution

CDC6 induction

OFF ON

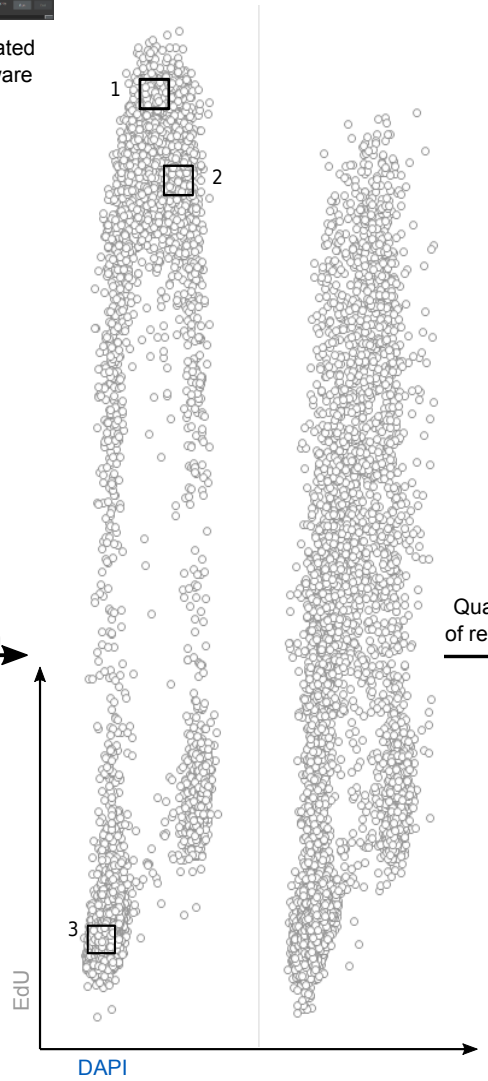

Step 2

Quantification of repair events

CDC6 induction

OFF ON

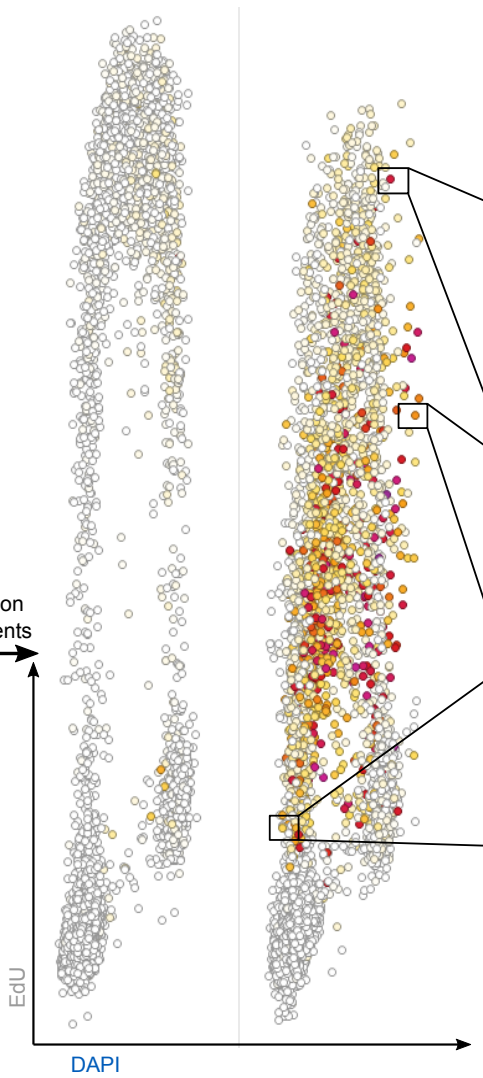

Color by RPA70 Counts

125
80
40
30
15
0

Spot detection (foci formation)

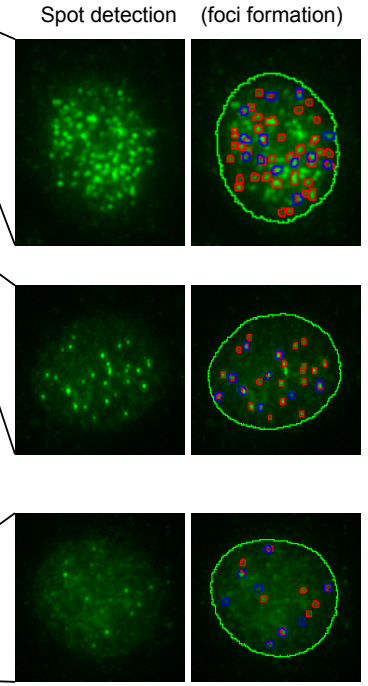

Step 3

Figure S3

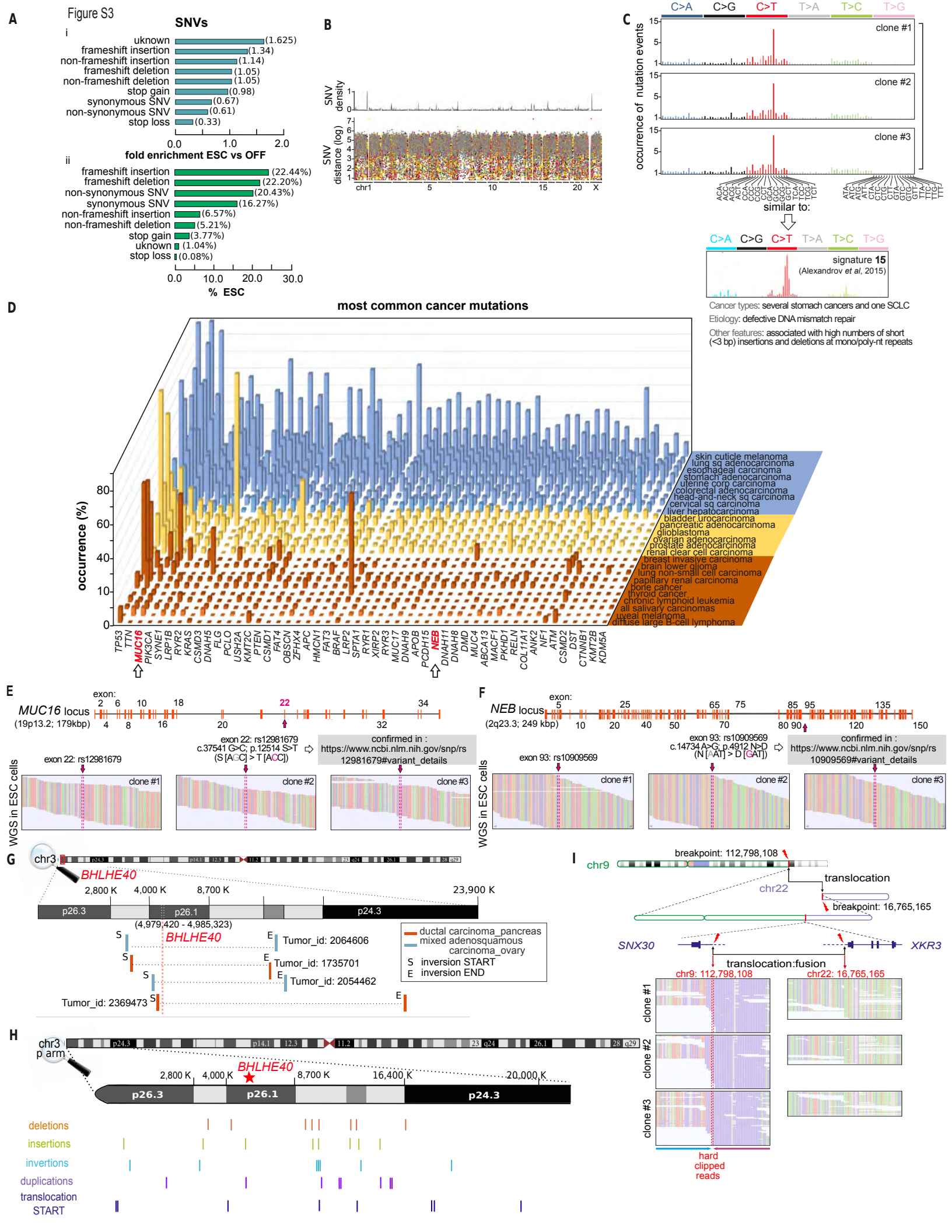
A
i
SNVs
uknown (1.625)
frameshift insertion (1.34)
non-frameshift insertion (1.14)
frameshift deletion (1.05)
non-frameshift deletion (1.05)
stop gain (0.98)
synonymous SNV (0.67)
non-synonymous SNV (0.61)
stop loss (0.33)
0.0 1.0 2.0
fold enrichment ESC vs OFF
ii
frameshift insertion (22.44%)
frameshift deletion (22.20%)
non-synonymous SNV (20.43%)
synonymous SNV (16.27%)
non-frameshift insertion (6.57%)
non-frameshift deletion (5.21%)
stop gain (3.77%)
uknown (1.04%)
stop loss (0.08%)
0.0 10.0 20.0 30.0
% ESC
B
SNV density
SNV distance (log)
chr1 5 10 15 20 X
C
C>A C>G C>T T>A T>C T>G
occurrence of nutation events
clone #1
clone #2
clone #3
similar to:
signature 15
(Alexandrov et al, 2015)
Cancer types: several stomach cancers and one SCLC
Etiology: defective DNA mismatch repair
Other features: associated with high numbers of short (<3 bp) insertions and deletions at mono/poly-nt repeats
D
most common cancer mutations
occurrence (%)
skin cuticle melanoma
lung sq adenocarcinoma
esophageal carcinoma
stomach adenocarcinoma
uterine corp carcinoma
colorectal adenocarcinoma
head-and-neck sq carcinoma
cervical sq carcinoma
liver hepatocarcinoma
bladder urocarcinoma
pancreatic adenocarcinoma
glioblastoma
ovarian adenocarcinoma
prostate adenocarcinoma
renal clear cell carcinoma
breast invasive carcinoma
brain lower glioma
lung non-small cell carcinoma
papillary renal carcinoma
bone cancer
thyroid cancer
chronic lymphoid leukemia
all salivary carcinomas
uveal melanoma
diffuse large B-cell lymphoma
TP53 TTN MUC16 PIK3CA SYNE1 LRP1B RYR2 KRAS CSMD3 DNAH5 FLG PCLO USH2A KMT2C PTEN CSMD1 FAT4 OBSCN ZFHX4 APC HMCN1 FAT3 BRAF LRP2 SPTA1 RYR1 XIRP2 RYR3 MUC17 DNAH9 APOB PCDH15 NEB DNAH11 DNAH8 DMD MUC4 ABCA13 MACF1 PKHD1 RELN COL1A1 ANK2 NF1 ATM CSMD2 DST CTNNB1 KMT2B KDM5A
E
MUC16 locus
(19p13.2; 179kbp)
exon 22: rs12981679
exon 22: rs12981679 c.37541 G>C; p.12514 S>T (S [AGC] > T [ACC])
confirmed in : https://www.ncbi.nlm.nih.gov/snp/rs12981679#variant_details
WGS in ESC cells
clone #1
clone #2
clone #3
F
NEB locus
(2q23.3; 249 kbp)
exon 93: rs10909569
exon 93: rs10909569 c.14734 A>G; p.4912 N>D (N [AAT] > D [GAT])
confirmed in : https://www.ncbi.nlm.nih.gov/snp/rs10909569#variant_details
G
chr3
BHLHE40
2,800 K 4,000 K 8,700 K 23,900 K
p26.3 p26.1 p24.3
(4,979,420 - 4,985,323)
Tumor_id: 2064606
Tumor_id: 1735701
Tumor_id: 2054462
Tumor_id: 2369473
ductal carcinoma_pancreas
mixed adenosquamous carcinoma_ovary
S inversion START
E inversion END
H
chr3 p arm
2,800 K 4,000 K 8,700 K 16,400 K 20,000 K
deletions
insertions
invertions
duplications
translocation
START
I
chr9
breakpoint: 112,798,108
translocation
chr22
breakpoint: 16,765,165
SNX30
XKR3
translocation:fusion
chr9: 112,798,108
chr22: 16,765,165
clone #1
clone #2
clone #3
hard clipped reads

Figure S4

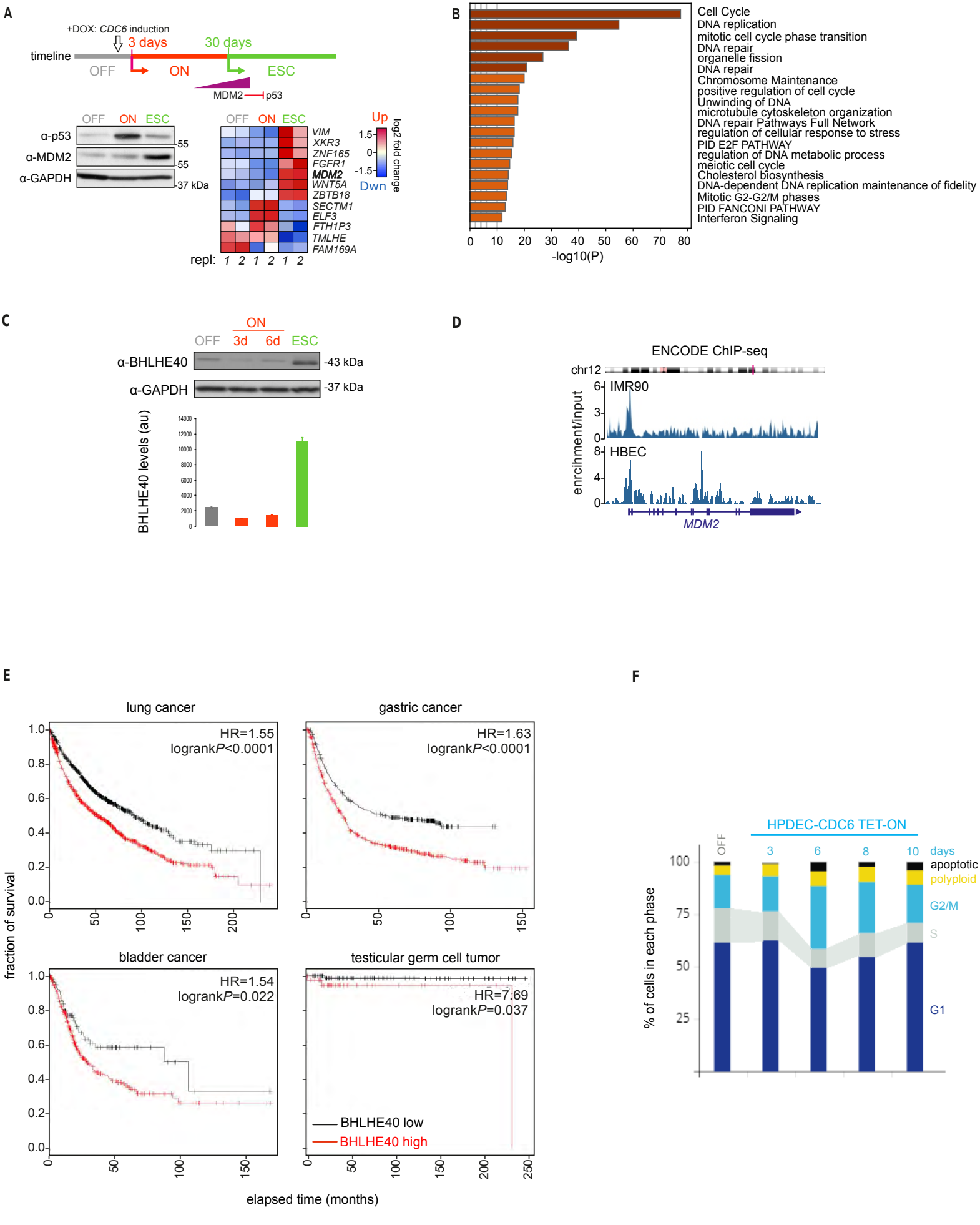
A
+DOX: CDC6 induction
3 days
30 days
timeline
OFF
ON
ESC
MDM2
p53
OFF ON ESC
α-p53
α-MDM2
α-GAPDH
55
55
37 kDa
OFF ON ESC
VIM
XKR3
ZNF165
FGFR1
MDM2
WNT5A
ZBTB18
SECTM1
ELF3
FTH1P3
TMLHE
FAM169A
repl: 1 2 1 2 1 2
Up
1.5
0
-1.5
Dwn
log2 fold change
B
Cell Cycle
DNA replication
mitotic cell cycle phase transition
DNA repair
organelle fission
DNA repair
Chromosome Maintenance
positive regulation of cell cycle
Unwinding of DNA
microtubule cytoskeleton organization
DNA repair Pathways Full Network
regulation of cellular response to stress
PID E2F PATHWAY
regulation of DNA metabolic process
meiotic cell cycle
Cholesterol biosynthesis
DNA-dependent DNA replication maintenance of fidelity
Mitotic G2-G2/M phases
PID FANCONI PATHWAY
Interferon Signaling
0 10 20 30 40 50 60 70 80
-log10(P)
C
ON
OFF 3d 6d ESC
α-BHLHE40
α-GAPDH
-43 kDa
-37 kDa
BHLHE40 levels (au)
14000
12000
10000
8000
6000
4000
2000
0
D
ENCODE ChIP-seq
chr12
IMR90
HBEC
enrcihment/input
6
3
0
8
4
0
MDM2
E
lung cancer
HR=1.55
logrankP<0.0001
gastric cancer
HR=1.63
logrankP<0.0001
bladder cancer
HR=1.54
logrankP=0.022
testicular germ cell tumor
HR=7.69
logrankP=0.037
fraction of survival
1.0
0.8
0.6
0.4
0.2
0.0
0 50 100 150 200
0 50 100 150
0 50 100 150
0 50 100 150 200 250
BHLHE40 low
BHLHE40 high
elapsed time (months)
F
HPDEC-CDC6 TET-ON
OFF
3
6
8
10
days
apoptotic
polyploid
G2/M
S
G1
% of cells in each phase
100
75
50
25

Figure S5

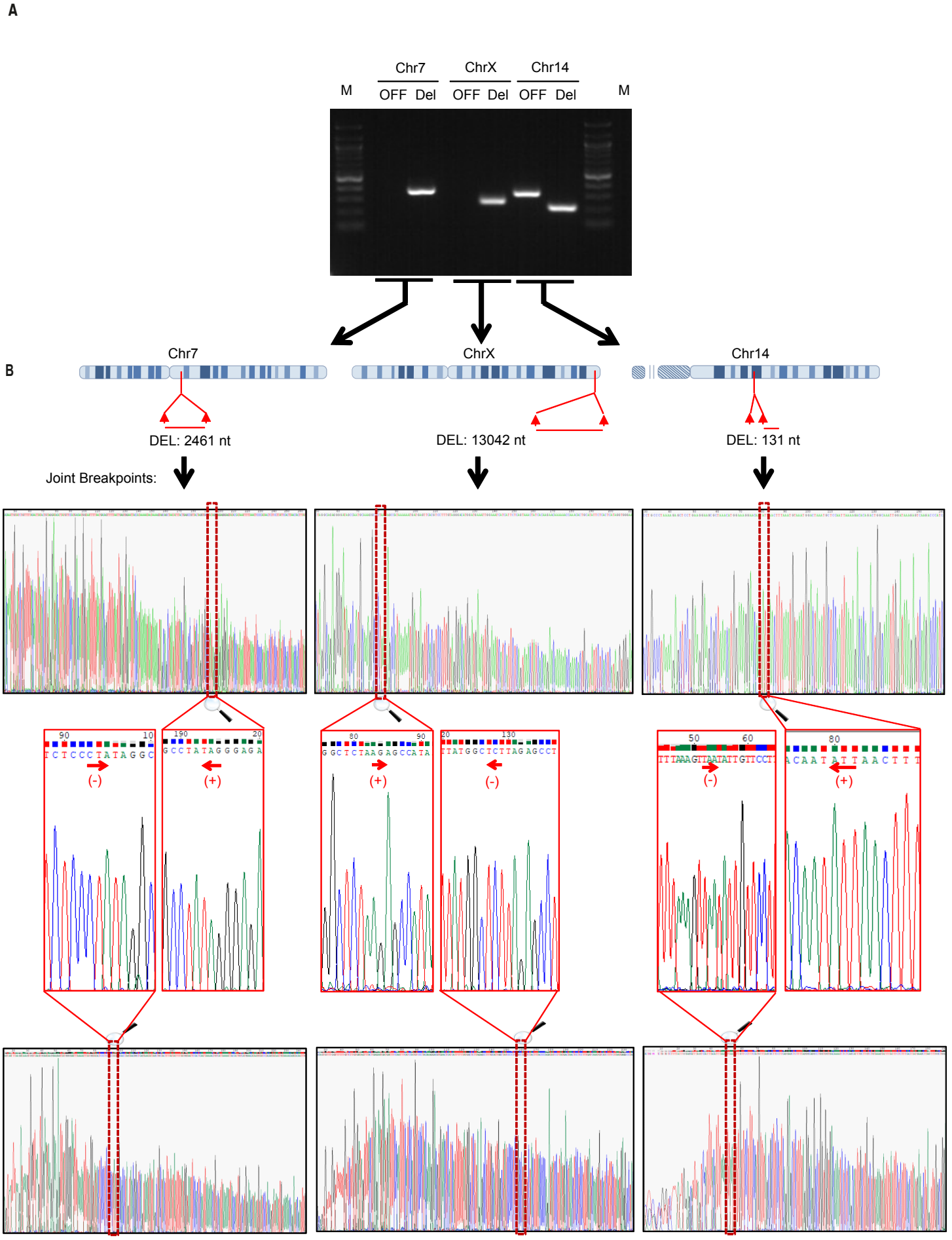
A
Chr7
ChrX
Chr14
M
OFF Del OFF Del OFF Del
M
B
Chr7
ChrX
Chr14
DEL: 2461 nt
DEL: 13042 nt
DEL: 131 nt
Joint Breakpoints:
Forward seq
Reverse seq
(-)
(+)
(+)
(-)
(-)
(+)

Figure S6

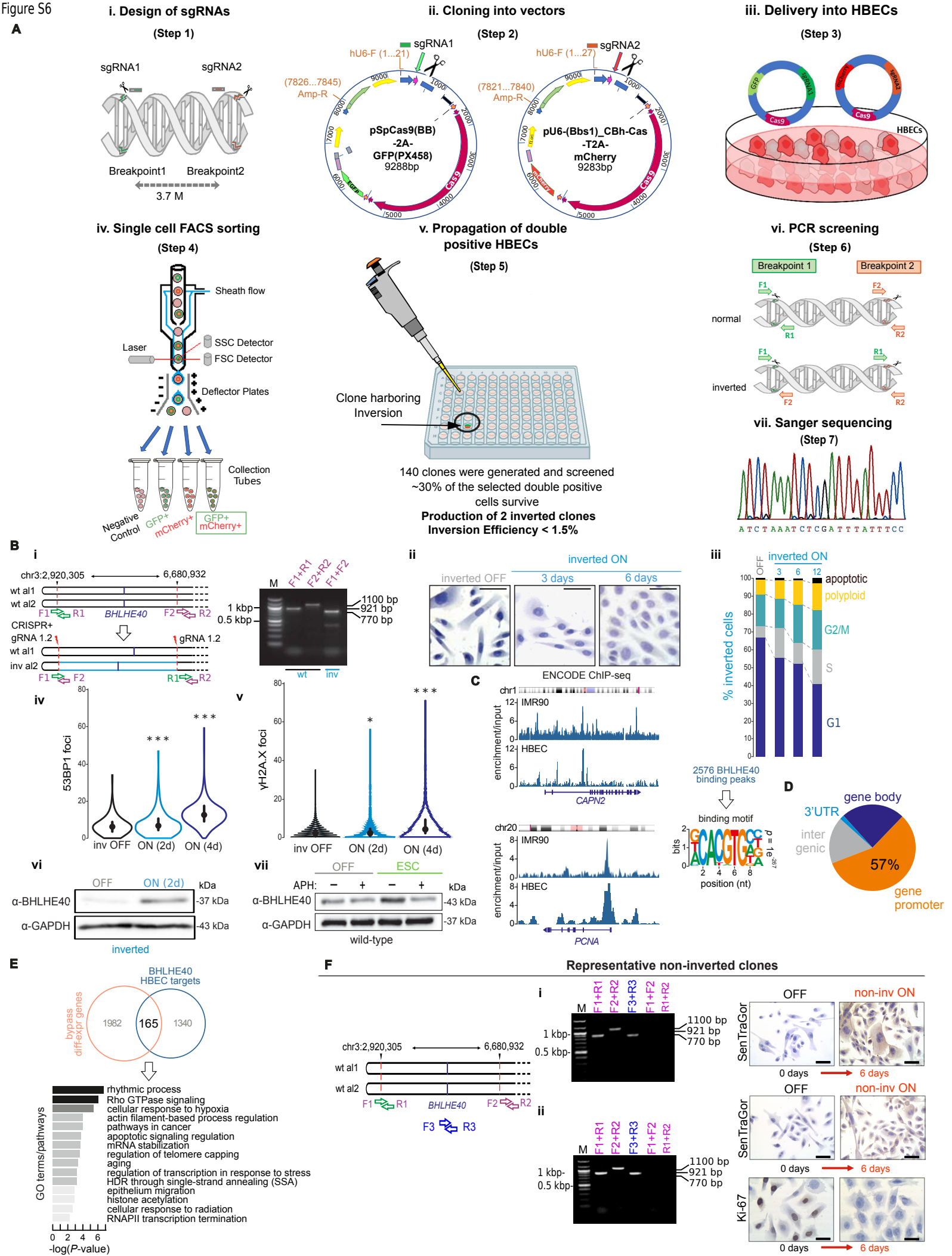
A
i. Design of sgRNAs
(Step 1)
sgRNA1
sgRNA2
Breakpoint1
Breakpoint2
3.7 M
ii. Cloning into vectors
(Step 2)
sgRNA1
hU6-F (1...21)
(7826...7845)
Amp-R
pSpCas9(BB)
-2A-
GFP(PX458)
9288bp
sgRNA2
hU6-F (1...27)
(7821...7840)
Amp-R
pU6-(Bbs1)_CBh-Cas
-T2A-
mCherry
9283bp
iii. Delivery into HBECs
(Step 3)
GFP
sgRNA1
mCherry
sgRNA2
Cas9
HBECs
iv. Single cell FACS sorting
(Step 4)
Sheath flow
Laser
SSC Detector
FSC Detector
Deflector Plates
Collection
Tubes
Negative
Control
GFP+
mCherry+
GFP+
mCherry+
v. Propagation of double
positive HBECs
(Step 5)
Clone harboring
Inversion
140 clones were generated and screened
~30% of the selected double positive
cells survive
Production of 2 inverted clones
Inversion Efficiency < 1.5%
vi. PCR screening
(Step 6)
Breakpoint 1
Breakpoint 2
normal
inverted
F1
F2
R1
R2
vii. Sanger sequencing
(Step 7)
ATCTAAATCTCGATTTATTTCC
B
i
chr3:2,920,305
6,680,932
wt al1
wt al2
BHLHE40
CRISPR+
gRNA 1.2
inv al2
M
1 kbp
0.5 kbp
1100 bp
921 bp
770 bp
wt
inv
ii
inverted ON
inverted OFF
3 days
6 days
iii
OFF
inverted ON
apoptotic
polyploid
G2/M
S
G1
% inverted cells
iv
53BP1 foci
inv OFF
ON (2d)
ON (4d)
v
γH2A.X foci
vi
OFF
ON (2d)
kDa
α-BHLHE40
-37 kDa
α-GAPDH
-43 kDa
inverted
vii
OFF
ESC
APH:
α-BHLHE40
-43 kDa
α-GAPDH
-37 kDa
wild-type
C
ENCODE ChIP-seq
IMR90
HBEC
enrichment/input
CAPN2
PCNA
2576 BHLHE40
binding peaks
binding motif
position (nt)
D
gene body
3'UTR
inter
genic
57%
gene
promoter
E
BHLHE40
HBEC targets
bypass
diffExpr genes
1982
165
1340
GO terms/pathways
rhythmic process
Rho GTPase signaling
cellular response to hypoxia
actin filament-based process regulation
pathways in cancer
apoptotic signaling regulation
mRNA stabilization
regulation of telomere capping
aging
regulation of transcription in response to stress
HDR through single-strand annealing (SSA)
epithelium migration
histone acetylation
cellular response to radiation
RNAPII transcription termination
-log(P-value)
F
Representative non-inverted clones
chr3:2,920,305
6,680,932
wt al1
wt al2
BHLHE40
F3
R3
i
ii
SenTraGor
Ki-67
OFF
non-inv ON
0 days
6 days

Figure S7

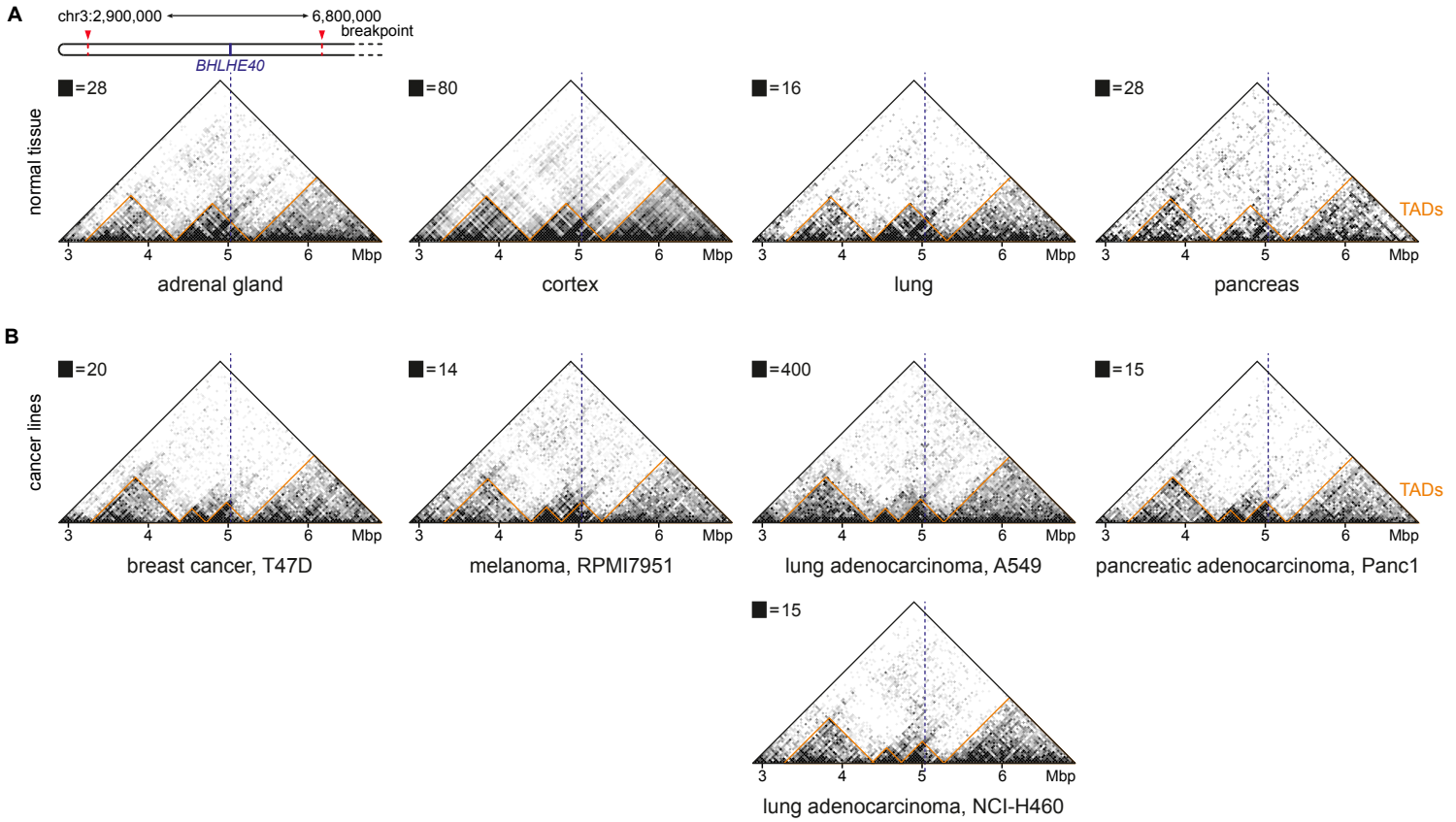
A
chr3:2,900,000
6,800,000
breakpoint
BHLHE40
normal tissue
■=28
■=80
■=16
■=28
TADs
3
4
5
6
Mbp
adrenal gland
cortex
lung
pancreas
B
cancer lines
■=20
■=14
■=400
■=15
TADs
breast cancer, T47D
melanoma, RPMI7951
lung adenocarcinoma, A549
pancreatic adenocarcinoma, Panc1
■=15
lung adenocarcinoma, NCI-H460

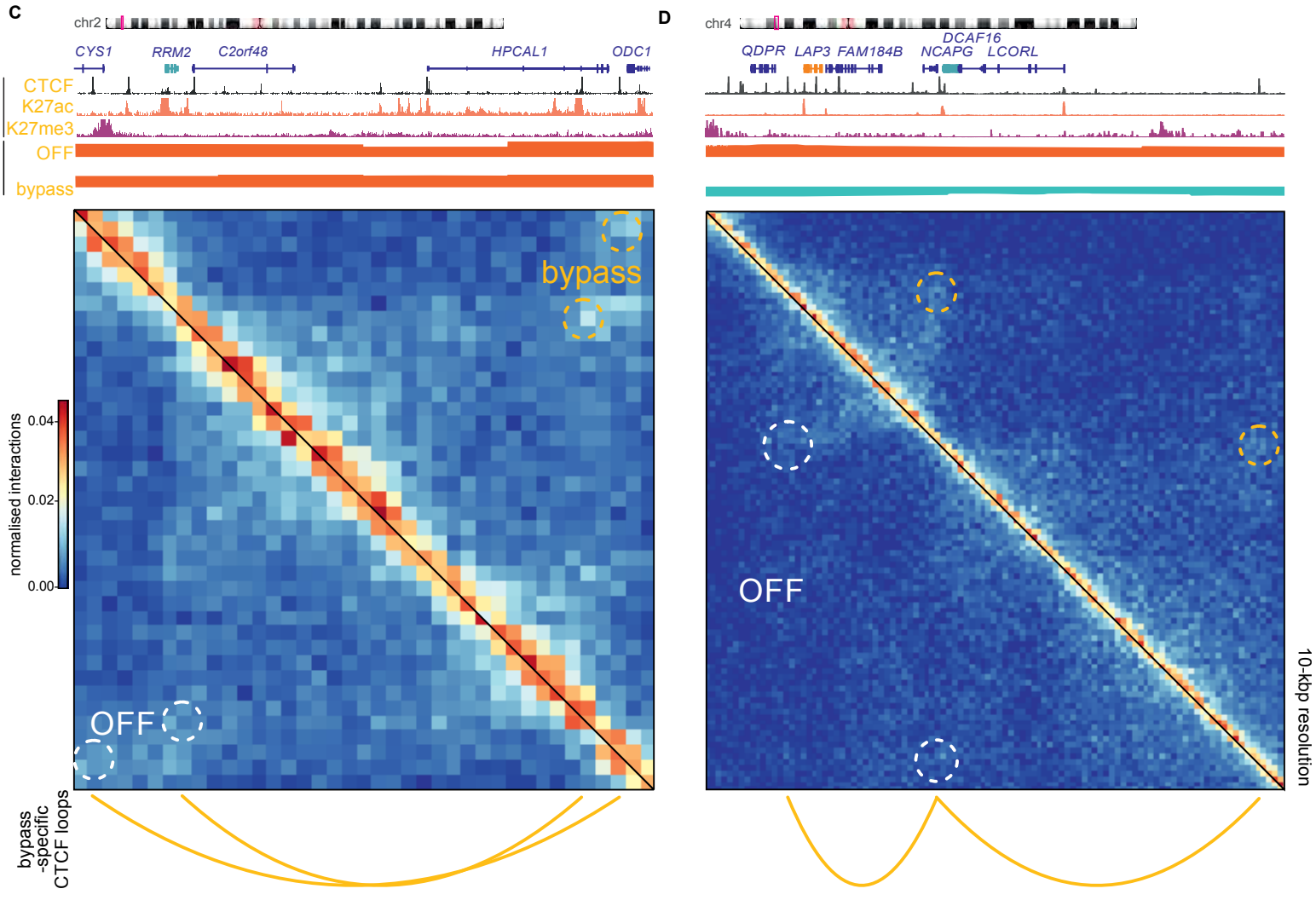
C
chr2
CYS1
RRM2
C2orf48
HPCAL1
ODC1
ChIP
CTCF
K27ac
K27me3
A/B
OFF
bypass
bypass
OFF
normalised interactions
0.04
0.02
0.00
bypass -specific CTCF loops
D
chr4
DCAF16
QDPR
LAP3
FAM184B
NCAPG
LCORL
OFF
10-kbp resolution

SUPPLEMENTAL FIGURE LEGENDS

Figure S1. *CDC6* overexpression is associated with poor survival of cancer patients and drives escape from oncogene-induced senescence. Related to Figure 1.

(**A**) Kaplan-Meier survival plots generated using public data from tumors stratified as "high" (*red line*) or "low" CDC6-expressing (*black line*; http://www.kmplot.com). Plots for breast and prostate tumors were generated using data from Metabric and TCGA, respectively.

(**B**) A human bronchial epithelial cell (HBEC) *CDC6*-Tet-ON cellular system recapitulating successive stages of cancer evolution [Komseli et al., 2018].

(**C**) Representative images of HBECs grown in 3D organotypic conditions and immunostained for H-E (hematoxylin-eosin), CDC6, GL13 (SenTraGor), and Ki-67 following the timeline in panel B. Non-induced cells (OFF) recapitulate the upper respiratory epithelium. Upon *CDC6* induction, cells enter senescence and form spheroids. Prolonged *CDC6* induction gives rise to ESC cells with an EMT phenotype (arrowheads) and renewed proliferative capacity (arrowhead in Ki-67-stained ESC cells) that invade the supporting collagen matrix (arrowheads in CDC6-stained ESC cells). Scale bar: 25 μm.

(**D**) Western blots showing changing levels of Dox-induced CDC6 in HBECs.

(**E**) Line plots quantifying sustained proliferation (mean ±S.D.; n=3) of ESC/CDC6-OFF cells. *: significantly different to OFF: $P<0.05$, unpaired two-tailed Student's t-test.

(**F**) As in panel **E**, but with bar plots quantifying cell invasion capacity.

Figure S2. Schematic depiction of quantitative image-based cytometry (QIBC) workflow. Related to Figures 2 and 3. This high-content fluorescent technique allows the measurement of different parameters of nuclear repair factors during the cell cycle. The experiment consists of 3 steps. Cells expressing Cdc6 in various timepoints (compared to the uninduced cells 'OFF') that are growing on coverslips are incubated with 5-ethynyl-2'-deoxyuridine (EdU), the nucleotide analog, for 30min before pre-extraction and fixation. As step1 of the method, clickit chemistry is performed and then cells are stained for DAPI and a specific DNA damage or/and Replication Stress-marker. Step 2 consists of the image acquisition using a fully-motorized automated wide-field microscope. Cells are plotted according to the cycle distribution based on DAPI and EdU signal and every dot represents a single cell. At the 3rd step, fluorescent signals associated with DNA damage- or/and RS-marker are quantified and expressed as a heat map (on the right corner of the 2nd set of plots). 5000 cells are analyzed for each condition typically. Scale bar, 10μm. Further specifications can be found in the methods section and as described previously [Toledo et al., Cell 2013].

Figure S3. CDC6-driven single nucleotide variant (SNVs) landscapes in ESC cells and publicly available alterations at chr3 in human malignancies. Related to Figure 4.

(**A**) Bar plots showing the type and relative enrichment, as fold (i) versus OFF and percentage (ii) of SNVs in ESC cells using WGS data.

(**B**) WGS-derived SNVs density plots aligned to a "kategis" SNV distribution in ESC genomes.

(**C**) Bar plots showing the occurrence of specific SNVs in each of the three independent replicates that represent a *CDC6*-specific mutational signature similar to that previously reported for stomach cancer and one small lung cell carcinoma [Alexandrov et al., 2013].
(**D**) Two of the top 50 most frequent mutations observed in cancer specimens in *MUC16* and *NEB* (*arrows*) were consistently recapitulated in our CDC6-driven cancer evolution model.
(**E**) *MUC16* encodes an established biomarker for diagnosis of many cancers, including lung (the origin of our HBEC model). The identified mutation maps to exon 22 (*arrow*) in a domain associated with protein stabilization and previously confirmed (see SNPdb: rs12981679).
(**F**) As in panel E, but for the *NEB* locus encoding the actin-binding protein nebulin with a mutation in exon 93 also previously confirmed in cancer (see SNPdb: rs10909569).
(**G**) Inversions affecting the *BHLHE40* locus in human malignancies.
Graph depicting recorded inversions in human tumors that encompass the *BHLHE40* locus.
(H) Map of previously reported genetic aberrations surrounding the *BHLHE40* locus.
Graph depicting various chromosome 3p alterations nearby the *BHLHE40* locus found in various human malignancies and extracted from public repositories (**Table S2**).
(**I**) A reciprocal translocation involving chr9 and 22 among the ESC-shared CNVs.
WGS data describing the translocation breakpoints in ESC cells connecting chr9 and 22 [Valencia et al., Advances in Hematology 2009; Chandran et al., Front Oncol 2019]. Hard clipped and discordantly mapped reads are indicated for all three replicates.

Figure S4. BHLHE40 gene targets in ESC cells and impact on tumor patients survival. Related to Figure 5.
(**A**) MDM2 is a BHLHE40 target upregulated in ESC cells. Western blots and RNA-seq data confirm *MDM2* upregulation and p53 suppression in ESC cells.
(**B**) Bar graphs from gene ontology and pathway analysis showing a log10 (*P* - value) enrichment of genes identified as both BHLHE40 targets and differentially expressed during escape (see also **Figure 5**; **Table S3**).
(**C**) Western blots showing changing BHLHE40 levels in OFF, ON and ESC cells.
(**D**) Genome browser views of BHLHE40 ENCODE ChIP-seq data from IMR90 and own data from HBECs cells showing binding to the *MDM2* locus.
(**E**) *BHLHE40* overexpression in malignancies is associated with poor survival.
Kaplan-Meier survival plots generated using available data (http://www.kmplot.com) from tumors stratified as “high” (red) or “low” BHLHE40-expressing.
(**F**) Cell cycle analysis in an HPDEC-based *CDC6*-Tet-ON system.
FACS-based cell cycle analysis of HPDECs demonstrating no absence of S-phase at different days after *CDC6* induction.

Figure S5. Sanger sequencing confirmed flanking breakpoints in representative shared CNVs. Related to Figure 4.
(**A**) Agarose gel (1.5%) electrophoresis of PCR products over shared deletions at chr7, chr 14 and chr X (see **Figure 4C** and **Table S1**). PCR reactions in OFF and ESC cells confirmed the deletions, while Sanger sequencing in ESC cells **(**see **B)** depicted the coordinates of

breakpoints. Note: due to the large size of the deleted fragments at chr7 and chr X, conventional PCR amplifications yielded no products in OFF cells.
(**B**) Sanger sequencing over flanking breakpoints at deletions found at chr7, chr 14 and chr X in ESC cells. Forward and reverse strand sequencing are depicted, along with magnifications at corresponding breakpoint junctions.
Note: full sequences can be found in **Table S4E**.

Figure S6. Flow diagram of method to generate and validate an inversion in the short arm of chr3 based on CRISPR/Cas-9 editing procedure and additional CRISPR-generated clones with or without the chr3 inversion. Related to Figure 6.
(**A**) CRISPR experimental strategy:
i. Design of sgRNAs near the breakpoints, as identified by WGS (72 bp from breakpoint 1 and 50 bp from breakpoint 2).
ii. Cloning of sgRNA1 and sgRNA2 into vectors expressing Cas9 and GFP or mCherry, respectively.
iii. Co-transfection of both vectors into HBECs.
iv. Single-cell FACS sorting to separate the double positive cells (GFP+/mCherry+).
v. Plating of double positive single cells in 96-well plates. Only 30% of the plated double positive cells finally survive.
vi. Design of primers around each breakpoint (F1/R1 around breakpoint 1 and F2/R2 around breakpoint 2) for PCR screening of the clones harboring the inversion. The inversion is identified by successful F1/F2 and R1/R2 amplification. Among the clones that survived and propagated, the inversion efficiency was less than 2%.
vii. Sanger sequencing validation is performed on the PCR products of the inverted clones.
(**B**) (i) PCR and Sanger sequencing (see **Table S4B**) validation of a second clone carrying a CRISPR-generated 3.7-Mbp heterozygous inversion in chr3 that closely mimics that discovered using WGS. (ii) Representative images of OFF and 3-/6-day ON "inverted" cells stained with SenTraGor and demonstrating senescence-bypass. Scale bar: 15 μm. (iii) FACS analysis of this "inverted" clone indicating increasing S-phase at different days after *CDC6* induction. (iv) Violin plots depicting 53BP1 foci accumulation upon *CDC6* induction in "inverted" cells. *: significantly different to OFF; $P < 0.05$, ***: significantly different to OFF; $P < 0.001$, unpaired two-tailed Student's t-test (±S.D.; n=3). (v) As in subpanel iv, but for γH2A.X foci. (vi) Western blots showing BHLHE40 overexpression upon *CDC6*-induction; GAPDH provides a loading control. (vii) As in subpanel vi, but showing the effect of aphidicolin (APH) treatment on BHLHE40 levels in wild-type OFF and ESC cells.
(**C**) Representative genome browser views of BHLHE40 ChIP-seq signal from IMR90 (ENCODE data) and HBECs (own data) in the CAPN2 and PCNA loci. The motif deduced from the 2576 ChIP-seq peaks matches the BHLHE40 one (*top right*).
(**D**) Pie chart showing genomic distribution of the BHLHE40 ChIP-seq peaks. 57% of peaks are promoter-proximal.
(**E**) Venn diagram (*top*) showing the overlap of BHLHE40 gene targets in "inverted" HBECs with genes differentially-expressed upon senescence bypass. This overlap is more than expected by chance (hypergeometric test; *P*-value < 10^{-6}). The GO terms/pathways

associated with these 165 genes are presented as a bar graph of enrichment *P*-value (-log; *bottom*).

(**F**) Representative (i,ii) PCR verified 6-day ON "non-inverted clones" cells stained with SenTraGor demonstrating senescence and no proliferation (negative Ki-67 immunostaining). Scale bars: 25 µm for SenTraGor and 20 µm for Ki-67 staining, respectively.

Figure S7. TAD organization in the extended *BHLHE40* domain and Changes in 3D chromatin looping explain *CDC6*-induced gene deregulation. Related to Figure 7.

(**A**) Hi-C interactions using public data from four normal tissues via the 3D Genome browser (http://promoter.bx.psu.edu/hi-c/view.php) in the 3.9 Mbp around *BHLHE40* (*dotted line*) at 40-kbp resolution. The positions of TADs (*orange triangles*) are also indicated.

(**B**) As in panel A, but for the indicated cancer cell lines.

(**C**) Hi-C heatmaps showing interaction changes between OFF and bypass "inverted" cells in the extended *RRM2* locus on chr2 are shown aligned to CTCF, H3K27ac and H3K27me3 ChIP-seq data, A/B-compartments, and CTCF loop positions. Bypass-specific loops emerging are indicated (*dotted circles*).

(**D**) As in panel A, but for the *LAP3*/*NCAPG* locus on chr4.